Tunneling nanotubes propagate a BMP-dependent preneoplastic state.

Cristina Cuella Martin[1,2,3], Thanh Thuy Nguyen *[1,2,3], Alexia Bertin *[1,2,3], Kevin Geistlich[1,2,3,4], Boris Guyot[1,2,3], Sylvain Lefort[1,2,3], Emmanuel Delay[1,2,3,4], Charline Dalverny[3,5], Alice Boissard[6], Cécile Henry[6], François Guillonneau[6,7,8], Eve-Isabelle Pécheur §*[1,2,3] and Véronique Maguer-Satta §*[1,2,3,4]

1. CNRS UMR5286, Centre de Recherche en Cancérologie de Lyon, 69008 Lyon, France;
2. Inserm U1052, Centre de Recherche en Cancérologie de Lyon, 69008 Lyon, France;
3. Université Claude Bernard Lyon 1, Lyon, France;
4. Centre Léon Bérard, 69008 Lyon, France;
5. Centre Technologique des Microstructures (CTμ), 69622 Villeurbanne, France;
6. Prot'ICO proteomics facility, Institut de Cancérologie de l'Ouest, 49055 Angers, France,
7. Nantes Université, Inserm, CNRS, CRCI2NA, U1307, UMR6075, 44000 Nantes, France;
8. Equipe Labellisée Ligue Contre le Cancer, Paris, France.

* These authors contributed equally; § Co-corresponding authors

Co-corresponding authors: Eve-Isabelle PÉCHEUR and Véronique MAGUER-SATTA, Centre de Recherche en Cancérologie de Lyon-CRCL, UMR CNRS 5286/Inserm U1052, 28 rue Laënnec, 69373 Lyon Cedex 08, France; 33-4-7878-2907 or 33-4-7878-2806.
Emails: eve-isabelle.pecheur@inserm.fr ; veronique.maguer-satta@lyon.unicancer.fr

Keywords: Tunneling nanotubes, cell communication, preneoplasia, BMP, luminal breast tumor initiation, stem cells.
Word count : 3321.

Abstract.

Tunneling nanotubes (TNTs) are thin, actin-based structures allowing long-distance communication between cells through the transfer of molecules and organelles. Although well-known to contribute to cancer progression, their role in early tumor initiation remains as yet unexplored. Here we address this question by using normal human mammary primary cells and an in-house human breast cell model recapitulating early luminal breast transformation. TNTs become more abundant and elongated during this process, and preferentially connect transformed donor cells to non-transformed acceptor cells. We show that this long-range directional communication involves the transfer of the signaling receptor BMPR1b. Within days, this transfer induces gene expression changes in acceptor cells, consistent with early transformation programs. Functional analyses of these acceptor cells revealed phenotypic changes, including anchorage-independent growth. In particular, the transferred BMPR1b receptor sensitized acceptor cells to BMP2 signals present in the microenvironment, amplifying their transformation potential. Hence, by tracking the earliest molecular responses in acceptor cells, we deciphered the initial steps of a transformation cascade triggered by TNT-mediated transfer. These findings uncover a BMP-dependent mechanism by which transformed cells propagate a preneoplastic state to adjacent and distant cells at the very onset of transformation, offering new perspectives on how epithelial transformation arises and spreads to neighboring cells.

With 2.3 million women affected worldwide and 700,000 deaths per year, breast cancer is the leading cause of cancer-related death in women, with luminal types representing 70% of all cases (*1*), and ductal carcinoma *in situ* (DCIS) the earliest non-invasive stage. The Bone Morphogenetic Proteins (BMP) pathway is a key actor altered during luminal breast tumorigenesis (*2–4*). Together with an interleukin-6 (IL6)-mediated inflammation, enhanced BMP2 secretion by the niche surrounding mammary stem cells fuels their transformation into cancer stem cells *via* amplification of their response to the kinase BMP receptor type 1b (BMPR1b), without detectable genetic alterations (*3*, *5*). Cancer stem cells can drive tumorigenesis and chemoresistance through exogenous signaling pathways that maintain their stemness and promote survival (*6*, *7*). BMPR1b-silenced transformed mammary cells have drastically decreased capacities to initiate tumor formation *in vivo* (*3*). However, the early dynamics of BMP-mediated transformation and the evolution of non-transformed mammary cells towards tumor cells remain unexplored.

Tunneling nanotubes (TNTs) are thin, transient actin-based structures enabling long-range intercellular communication (*8*, *9*), *via* the transfer of organelles, small molecules, proteins and nucleic acids. TNTs have been implicated in tumor progression, metastasis, and chemoresistance. Cancer cells linked to neurons by TNTs exhibited enhanced metastatic capacities (*10–12*). Yet the role of TNTs at earliest stages of tumorigenesis is unknown.

While BMPs and TNTs have independently been associated with breast cancer, their potential interaction is unexplored. Also, the nature, directionality, and functional consequences of cell/cell communications at the tumor initiation stage remain ill-defined.

In this work, we aimed to delineate the interplay between the BMP pathway and TNT-mediated communication, to shed light on the earliest steps of transformation of (immature) mammary cells.

71 **Results.**

72 **TNT formation during mammary epithelial stem cells transformation.**

73 Early BMP-driven transformation dynamics was explored by using our MCF10A-derived stem
74 cell models obtained by chronic exposure to IL6 and BMP2 (MC26 and M1B26; Fig. 1A) (*3*,
75 *5*). Sorting of BMPR1b-expressing cells prior to cytokine treatment, followed by soft agar
76 clones selection, led to quicker establishment of transformed cells (M1B26), with greater *in*
77 *vitro* anchorage-independent growth and *in vivo* engraftment than in non BMPR1b-sorted cells
78 (MC26). These models display DCIS molecular features and robustly recapitulate the *in vivo*
79 BMP pathway alterations (*3, 5)*. Confocal microscopy observations of non-transformed control
80 (MCF10A-CT) and transformed cells (MC26, M1B26) revealed long-range contacts *via* long
81 thin F-actin-rich TNTs (*13*) (Fig. 1B). Although TNT quantification requires low-confluence
82 cultures (*14*), long-range TNTs were also detectable at high cell density (Fig. S1A).
83 Transformed cells exhibited over twice as many TNTs as non-transformed cells (Fig. 1C, left).
84 The proportion of long TNTs increased ~fivefold with transformation (Fig. 1C, right). However,
85 TNT average length did not differ between cell lines (Fig. S1B). Neither TNT number nor length
86 varied in non-transformed cells exposed to conditioned medium of transformed ones (Fig. S1B-
87 D). TNTs in transformed cells were often branched, with ramifications and bulges (Fig. 1D
88 black arrow) (*8*, *13*). While most TNTs were open-ended, allowing a cell-cell cytoplasmic
89 continuum (Fig. 1E), some close-ended TNTs featuring a Gap junction at one tip were seen
90 (Fig. S1E). TNTs did not adhere to the substrate and were observed within 3D structures such
91 as acini, basic functional units of breast glandular tissue (Fig. 1F; Fig. S1F). TNTs also
92 contained microtubules (*8*, *15*) (Fig. S1G), and mitochondria (*16*) (Fig. 1G; Fig. S1H).
93 Importantly, transformed cells could also establish TNT connections with non-transformed
94 primary fibroblasts (Fig. 1H) and epithelial mammary cells (Fig. 1I) isolated from healthy
95 human breast samples.

96 This indicates that early mammary cell transformation leads to an enhanced ability of
97 transformed cells to connect to their neighbors through TNTs.

98

99 **Directional transfer of cellular material *via* TNTs from transformed to non-transformed**
100 **cells.** To investigate how TNTs connect cells, we cocultured mCherry-expressing MCF10A-CT
101 with GFP-expressing M1B26 cells, seeded at low density (*14*). Both M1B26 transformed (Tf)
102 and MCF10A-CT non-transformed (NoTf) cells formed TNT structures, connecting Tf to Tf,
103 NoTf to NoTf and Tf to NoTf cells (Fig. 2A). Quantification of TNT contacts revealed that
104 connections were more frequent and abundant from Tf towards NoTf cells than in the opposite

105 direction (Fig. 2B,C). Fluorescent material from GFP-tagged Tf cells accumulated within the
106 cytoplasm of NoTf cells (Fig. 2D), suggesting a directional transfer *via* TNTs, Tf cells as donors
107 and NoTf cells as acceptors (Fig. 2E; Movie S1; Fig. S2A). To assess the proportion of cellular
108 exchange between cells, mCherry-NoTf cells were cocultured with GFP-Tf cells for 8 days.
109 Flow cytometry analysis revealed a higher proportion of mCherry-NoTf cells exhibiting green
110 fluorescence uptake compared to GFP-Tf cells acquiring red fluorescence (Fig. S2B), indicating
111 a preferential Tf-to-NoTf directional transfer (Fig. 2F-H). Switching fluorophores between Tf
112 and NoTf cells yielded similar results (Fig. S2C,D), and this directional transfer increased over
113 time (Fig. S2E-I). When using normal human primary mammary cells as NoTf cell sources, we
114 also observed a Tf-to-NoTf directional material transfer in coculture (Fig. 2J,K), as with
115 MCF10A-CT cells (Fig. S2J). To evaluate the contribution of cell-cell communication through
116 secretion of soluble compounds and extracellular vesicles, we performed cultures of normal
117 human primary cells: (i) with Tf cells separated by a physical barrier (Transwell™), to impede
118 TNT formation; (ii) in Tf cells conditioned medium (CM, schematic Fig. 2I). In the former
119 condition, the number of acceptor cells dropped in both transfer directions (Fig. 2J,K; Fig. S2J).
120 In the latter, no fluorescence exchange *via* soluble components was observed (Fig. S2K,L).
121 Therefore, directional material transfer preferentially occurs *via* TNTs from Tf to NoTf cells,
122 and rather than through other forms of cell-cell communication.
123

124 **TNT-mediated transfer modulates proteomic features of acceptor cells.**
125 Fluorescently-labeled cells cultured for 8 days (Fig. 3A), were sorted by flow cytometry into
126 four populations: non-transformed (NoTf), transformed (Tf), non-transformed cells that
127 received fluorescent material (NoTf accept), and non-transformed cells from the same coculture
128 that did not receive any material (NoTf no accept). Unbiased proteomic screening of each
129 population followed by gene enrichment pathway analysis revealed that most enriched
130 pathways in NoTf accept, compared to NoTf no accept of the same coculture, were related to
131 transport (organic/nitrogen compounds, protein, transmembrane, intracellular), and to
132 localization of intracellular organelles, macromolecules and proteins (Fig. 3B). Other pathways
133 pointed to mitochondrion organization and activity. Volcano plot analysis revealed that NoTf
134 accept were statistically distinct from NoTf no accept cells of the same coculture, and from
135 NoTf in monoculture (Fig. 3C; Fig. S3A). Of note, the most overexpressed proteins in the
136 former phenotype were involved in lipid metabolism and transport (*ATP8B1, RAB6B, CES1* –
137 EST1, *MEST*, *PIGA*), intracellular membrane and secretory vesicle trafficking (*RAB6B,*

138 *RAB11B, SYT8, CAV2, TMEM167A*), cell growth and morphology maintenance (*TRIQK*),
139 membrane protrusion formation (*ATP8B1*) and actin filament bundling (*LCP1* – Plastin-2)
140 (Table S1). Other overexpressed proteins were linked to mitochondrial activities (*COX7C*,
141 *MALSU1*), possibly related to the presence of mitochondria within TNTs (Fig. 1G; Figs. S1H,
142 S3B).
143 Six proteins, EST1, Plastin-2, Rab-6B, TRIQK, MEST and MASU1, were markedly
144 overexpressed in NoTf accept compared to NoTf no accept cells from same cocultures (Fig.
145 3D; Fig. S3C). Corresponding RNA levels were also enhanced in Tf compared to NoTf cells
146 (Fig. S3D). The TNT-mediated transfer of material therefore induces in acceptor cells
147 transcriptional and translational upregulation of key actors involved in progression towards a
148 transformed-like phenotype. This aligns with the downregulation of DAP1 (*DAP*) and thymosin
149 β-10 (*TMSB10*), respectively involved in ribosome hibernation and actin polymerization
150 inhibition (Table S1).
151 When TNT formation was physically impeded, acceptor cells showed phenotypic differences
152 compared to those in direct coculture (Table S2), but remained comparable to NoTf cells in
153 monoculture (Fig. S3E,F). Notably, NoTf accept cells from direct cocultures exhibited a higher
154 expression of early inflammatory markers (*SERPINA3, CD14*) and motility-related genes
155 (*IGFBP6*) than their Transwell™ counterparts. These findings indicate that TNT-mediated
156 direct contacts with transformed cells induce profound changes in the proteomic landscape of
157 non-transformed acceptor cells, similar to those observed in early transformed cells.
158 Ras-driven oncogenic transformation being a well-established process, we next investigated
159 whether it could also promote the formation of TNTs. Proteomics revealed a marked increase
160 in H-Ras and K-Ras oncoproteins in NoTf accept cells compared to NoTf cells in monoculture
161 (Fig. 3E). We then examined two additional models involving Ras-mediated transformation of
162 mammary epithelial cells. First, in the Weinberg's model of human mammary epithelial cells
163 immortalized with SV40-L antigen and hTERT, then transformed with H-Ras (*17*), TNTs were
164 present in malignant and non-malignant cells, with shorter TNTs in the former (Fig. 3F,H).
165 Second, in H-Ras-transformed immature MCF10A-derived AT1 and DCIS cells, malignant
166 cells exhibited fewer TNTs than non-malignant ones, without length difference (Fig. 3G,I).
167 Hence, Ras-induced transformation does not enhance long-distance TNT-mediated
168 communication, contrary to clinically relevant inflammation- and BMP-driven mechanisms (*3*).
169
170
171

TNT-mediated transfer impacts the BMP pathway of recipient cells.

Since transmembrane and protein transports were the most impacted processes (Fig. 3B), and given that the BMP pathway is a key driver of luminal transformation (*3*, *4*) (Fig. S4A,B), we examined whether this pathway was affected in non-transformed acceptor cells. We focused on the canonical SMAD cascade, and among non-canonical MAPK downstream cascades, on p38 (MAPK14), because the p-p38/p38 ratio exhibited the highest level of expression in Tf cells (Fig. S4A,B). Eight target or regulator proteins of these cascades were extracted from our proteomic screening (Table S3), and assessed for their expression across sorted cell populations post-TNT connections (Fig. 3A). Several proteins involved in the BMP pathway — including ID1, Nup214 (*18*), spartin, and USP15 (*19*) — were consistently up- or down-regulated in NoTf acceptor cells, reaching levels comparable to those observed in Tf cells, exclusively after TNT transfer (Fig. 4A). ATF2, a transcription regulator positioned at the BMP pathway/p38 cascade interface, was underexpressed in NoTf acceptor cells, at levels comparable to those in Tf cells. Components of the p38 cascade were markedly altered following TNT-mediated transfer: MAPKAPK2, a kinase activated by p38 phosphorylation, was underexpressed in NoTf acceptor cells, consistent with the role of p38 inhibition in facilitating mammary tumorigenesis (*20*). Conversely, Rac1—part of a complex involved in actin bundling and stabilization, regulated by p38—was overexpressed in NoTf cells that received material *via* TNTs (Fig. 4A). BMPR1b expression increased with transformation, and the receptor was localized within TNTs, particularly in bulges, in normal primary and model mammary cells (Fig. 4B). This was concomitant to the activation of both canonical p-SMAD1/5/8 / SMAD1/5/8, and non-canonical p-p38/p38 and p-ERK/ERK cascades (Fig. S4A,B). Correlative light (scanning) electron microscopy (CLEM) enables to distinguish intra- from extra-cellular epitopes by overlaying optical and scanning electron images of the same region. Confocal imaging revealed a continuum of BMPR1b in cell bodies, as well as in or on TNTs. However, electron microscopy did not reveal any extracellular BMPR1b epitopes at TNTs (Fig. 4C). This suggests an extracellular localization in the cell body and an intraluminal presence in TNTs, consistent with BMPR1b trafficking through/within TNTs. Although incomplete (Fig. 4D,E top), *BMPR1b* silencing in Tf cells drastically reduced TNT number, and abolished the formation of long TNTs (Fig. 4E bottom). Silencing of G protein-coupled estrogen receptor 1 (*GPER*) was used as control, since no report linked GPER to TNT formation/function. Though more efficient than *BMPR1b* silencing (Fig. 4E top), *GPER* knockdown had no effect on TNT number or length (Fig. 4D,E bottom). Therefore, BMPR1b contributes to the formation and elongation of (long) TNTs.

To evaluate whether BMPR1b transfer *via* TNTs could sensitize NoTf cells to a BMP2/IL6-enriched microenvironment, the four sorted cell populations (Figs. 3A, 4F) were analyzed for BMPR1b mRNA expression. It was found ~8-fold higher in NoTf accept cells previously connected *via* TNTs, compared to an only ~2-fold increase when TNT formation was blocked (Fig. 4G). This supports a role for a TNT-mediated activation of the BMP pathway.

These findings underscores BMP pathway activation in NoTf cells acceptor of material from Tf cells, *via* TNT-mediated transfer. BMPR1b plays a dual role by promoting TNT formation and being transferred to acceptor cells.

TNT-trafficked BMPR1b sensitizes acceptor cells to a transforming microenvironment.

Long-term impact of BMPR1b transfer was assessed on sorted cells, cultured for up to 16 weeks with or without BMP2/IL6, mimicking *in vivo* luminal breast tumor conditions (*2)* (Fig. 4F). BMPR1b protein levels rose between weeks 6 and 10 before stabilizing, in NoTf accept cells exposed to cytokines after sorting (Fig. 5A left), reaching the highest expression among all populations by week 14 (Fig. 5A right; Fig. S4C,D). Accordingly, p-SMAD1/5/8 / SMAD1/5/8 and p-p38/p38 cascades were activated upon 4 to 6 week-exposure to BMP2/IL6 in NoTf accept cells (Fig. 5B,C; Fig. S4E,F). While the SMAD cascade did not return to baseline over weeks (Fig. 5B), the p38 cascade, after a strong activation as early as 4 weeks with cytokines post-sorting, reached baseline levels after 10 weeks (Fig. 5C).

We then cross-referenced our proteomic and transcriptomic datasets (*5*), and identified three tumor-associated genes significantly upregulated during transformation: *HOXB6* (*21*), *CCND2* (*22*), and *EREG* (*23*) (Fig. 5D). Their mRNA levels were increased in NoTf acceptor cells connected through TNTs with Tf cells, compared to NoTf cells in monoculture, and to NoTf acceptor cells for which TNT formation was blocked (Fig. 5E). This supports the notion that TNT-mediated transfer may promote a shift towards a preneoplastic state. HoxB6, Cyclin D2 and (pro)-epiregulin protein levels also tended to increase with transformation (Fig. S5A). *HRAS* was overexpressed in NoTf acceptor cells, further substantiating a shift towards a preneoplastic status (Fig. 4E). However, *HRAS* was neither involved in TNT formation, nor in TNT-mediated preneoplastic switch of acceptor cells (Fig. 3F-I). As a negative control, we selected *UFM1*, a gene involved in endoplasmic reticulum stress, a cellular insult suggested to contribute to TNT development (*24*). *UFM1* transcript levels remained unchanged regardless of transformation status or material uptake (Fig. S5B,C), indicating that although ER stress may be present, it is not a key driver of the cellular behavior described here.

239 NoTf acceptor cells grown with cytokines up to 16 weeks post-TNT transfer and sorting (Fig.
240 S6A), displayed anchorage-independent growth at earlier time points than other types of sorted
241 cells, and with a number of clones obtained comparable to that of Tf cells (Fig. 5F; Fig. S6B).
242 Potential cross-contamination between Tf and NoTf sorted cell samples was ruled out based on
243 the specific fluorescence of derived soft agar clones (Fig. S6C). All these features are hallmarks
244 of a preneoplastic transformation, observed exclusively in cells that had established TNT
245 contacts with transformed cells prior to sorting, enabling the transfer of transforming
246 information. BMPR1b, trafficked *via* TNTs from Tf to NoTf cells, thus emerges as a key
247 mediator of this process.
248 Hence, these findings unravel the key role of the BMP pathway in driving the preneoplastic
249 switch in NoTf cells receiving material from Tf cells through TNT-mediated transfer. TNT
250 communication would prime non-transformed cells to respond to a tumor-promoting
251 microenvironment, ultimately contributing to the propagation of transformation (Fig. 5G).
252

253 **Discussion**

254 Our findings reveal that TNT-mediated transfer of BMPR1b from transformed to non-
255 transformed cells activates BMP signaling in acceptor cells, sensitizing them to a tumor-
256 promoting microenvironment and initiating early features of transformation. The TNT-
257 mediated transfer of mitochondria from stromal to cancer (stem) cells has been well
258 documented (*25*), and recently, TNTs were shown to enhance the metastatic capacity of cancer
259 cells in primary tumors, receiving mitochondria from neurons (*10*).

260 In contrast, the delivery of material from transformed cells to non-transformed neighbors,
261 remains unexplored at very early stages of transformation. Our study is the first to investigate
262 the functional impact of TNT-mediated material exchange between cells of identical phenotype
263 (i.e. epithelial cells), on the predisposition of non-transformed cells to adopt a preneoplastic
264 status. Although donor-to-acceptor material transfer through secretion of soluble compounds
265 and extracellular vesicles occurred, it remained low to negligible, indicating that the processes
266 mainly relied on physical TNT-mediated communications. This directional transfer from
267 transformed to non-transformed cells leads within days to the overexpression of tumor-related
268 genes and of BMPR1b itself, evocative of a possible feedback loop that maintains transforming
269 conditions (Fig. 5G). Non-transformed cells also undergo profound changes in their proteomic
270 landscape, linked to transport processes, and within weeks acquire phenotypic traits of
271 preneoplasia, such as anchorage-independent growth, sustained BMPR1b overamplification
272 and related mounting of a non-canonical signaling cascade. The earliest events, within one
273 week, comprised the overexpression of *HOXB6*, *CCND2* and *EREG* by non-transformed
274 acceptor cells, after TNT contacts with transformed (donor) cells. Interestingly, upregulation of
275 these genes upon transformation has already been linked to other cancers: (i) *HOXB6*, encoding
276 a homeobox domain-containing transcription factor involved in development, is upregulated in
277 acute myeloid leukemia and osteosarcoma (*21*, *26*), with a possible role in cancer initiation
278 (*27*); (ii) *CCND2*, encoding cyclin D2, involved in DNA replication, cell division and cell cycle
279 regulation, was dysregulated in gastric, thyroid and colorectal cancers (*28*), and its
280 overexpression in breast cancer promotes MAPK-mediated cell proliferation and tumor growth
281 (*22*, *29*); (iii) upregulation of *EREG,* encoding the secreted protein ligand of the EGF receptor
282 (EGFR) epiregulin, is linked to breast cancer progression and resistance to tamoxifen by EGFR
283 activation (*23*, *30*).

284 Following TNT material transfer, including BMPR1b, *BMPR1B* becomes overexpressed in
285 acceptor cells within a week. The receptor molecule was detected within TNTs, overexpressed
286 in transformed cells, and structurally contributing to TNT elongation. As BMPR are known to
287 be located in lipid rafts, BMPR1b could induce TNT formation *via* its interaction with these
288 microdomains (*31*), from which TNTs might arise (*32*, *33*). These cholesterol-rich
289 microdomains provide high curvature and elasticity necessary for membrane deformation
290 linked to TNT formation. Cholesterol levels together with lipid rafts increase upon
291 transformation, as evidenced in prostate and breast cancer cell lines (*34*), further substantiated
292 by our proteomic data with acceptor cells displaying enhanced expression of EST1, a
293 carboxylesterase hydrolyzing cholesterol esters into free cholesterol. Additionally, BMP2 was
294 reported to promote actin polymerization via PI3Kα activation (*35*). We herein observed that
295 *LCP1* was upregulated upon transformation, concomitantly to its protein Plastin-2, in acceptor
296 cells following TNT transfer. Plastin-2 is a key actin-bundling protein involved in the formation
297 of cellular protrusions (*36*), overexpressed in epithelial-derived cancers including breast (*37*).
298 Its overexpression correlated with cancer cell migration, invasion, metastasis (*38*) and
299 chemoresistance (*39*). Plastin-2 activation depends on serine 5 phosphorylation *via*
300 ERK/MAPK, PI3K, and PKA/PKC pathways, enabling its recruitment to actin filaments and
301 promoting bundling and protrusion elongation, as shown in breast carcinoma (*40*). This agrees
302 with findings from the Zurzolo's group, showing that TNT induction by Eps8 involves its actin-
303 bundling activity (*41*). Altogether, this might explain the higher number of TNTs observed upon
304 transformation.

305 At the functional level, the analysis of acceptor cells sorted post-TNT transfer, revealed their
306 gradual transformation over weeks, faster and more extensively than non-acceptor cells,
307 concomitant to a progressive but sustained activation of the BMP pathway. This induced an
308 initial burst of p38 downstream response, followed by the prolonged activation of the canonical
309 SMAD cascade, only observed when TNT contacts existed. These recipient cells then exhibited
310 preneoplastic traits. Experiments on TNT-forming capacities of mammary cell models, where
311 transformation of either normal primary (*17*) or MCF10A cells (*42*) is « switched on » by the
312 H-Ras oncoprotein, showed fewer and shorter TNTs connecting cells. *HRAS* is overexpressed
313 in invasive breast tumors, but the prevalence of *HRAS* mutations in luminal types is negligible
314 (*1*, *43*). These mammary models do not faithfully recapitulate the earliest stages of non-invasive
315 luminal breast tumors triggered, for example, by exposure to carcinogenic cues such as
316 environmental pollutants, endocrine disruptors or alcohol (*3*, *44–46*).

317 Here, we unveil for the first time that TNTs transfer a signaling receptor, BMPR1b. This transfer
318 sensitizes acceptor cells to BMP2 signals of the microenvironment, rapidly triggering a cascade
319 of molecular events that culminate in phenotypic changes, with anchorage-independent growth
320 of previously non-transformed cells (Fig. 5G). Combined with the recent demonstration that
321 TNTs can transfer material *in vivo* (*47*), our work provides the foundation for a new concept:
322 the propagation, through TNTs, of a preneoplastic state within a population of initially non-
323 transformed mammary cells. This process could precede the development of luminal-type
324 tumors, and identify BMPR1b as a major early contributor of the BMP-dependent preneoplastic
325 switch of acceptor cells.

326

Data availability statement. The mass spectrometry proteomics data have been deposited to the ProteomeXchange Consortium via the PRIDE (https://www.ebi.ac.uk/pride/) (*48*, *49*) partner repository, with the dataset identifier PXD060023. Transcriptomic data have been deposited on the Gene Expression Omnibus repository, GSE18673411.

Acknowledgements. We thank P. Battiston-Montagne, M. Gautier and C. Vanbelle (CRCL, platform PIC), and D. Ressnikoff (SFR Santé Lyon Est, CIQLE). We thank the "AniRA lentivectors production facility" from the CELPHEDIA Infrastructure and SFR Biosciences, UAR3444/CNRS, US8/Inserm, ENS de Lyon, UCBL, especially G. Froment, D. Nègre and C. Costa. We thank J. Brocard, head of the LYMIC-PLATIM UAR 3444 / US8 microscopy platform (ENS Lyon, Univ Lyon 1), and E. Chatre. We thank B. Manship for english proofreading, P. Mehlen, P. Juin, R. Tomasini, C. Vérollet and B. Bartosch for inspiring discussions. Some illustrations were created in https://BioRender.com.
This work was supported by Agence Nationale de la Recherche (VMS, ANR-10-LABX-0061, ANR-CESA-018-04 and Convergence PLAsCAN ANR-17-CONV-0002); Ligue Nationale contre le Cancer (CCM, doctoral grant), Dept Ain, Rhône (VMS), Saône et Loire (EIP) ; Fondation ARC (CCM, 4th year doctoral grant; VMS, SFI20111203500, PJA20171206331) ; the ERiCAN program of Fondation MSD-Avenir (VMS/EIP, DS-2018-0015) and Associations [Déchaîne Ton Cœur (VMS); Ruban Rose Prix Avenir 2021 (VMS) ; Comité féminin pour le dépistage du cancer du sein 74 (VMS) ; Symatese Fondation (VMS), and Fondation pour la Recherche Médicale (équipe FRM EQU202203014695 VMS).

Contributions: V.M.S. and E-I.P designed and supervised the study, conceived methodological developments and acquired funding. V.M.S. provided administrative support. C.C.M., S.L. and B.G. collaborated in study design, contributed to methodological developments and data interpretations. K.G. performed RNA-seq and proteomic bioinformatic data analyses, and statistical gene-expression analyses. C.C.M., T.T.N., A.B. and E-I.P. performed and interpreted the experiments. C.D. designed and performed SEM and CLEM microscopy experiments. F.G., A.B. and C.H. performed proteomic analyses, and F.G. interpreted proteomic data. E.D. provided primary breast samples, and assisted with their processing. C.C.M., V.M.S and E-I.P. wrote the manuscript. All authors reviewed the manuscript and approved the final version for publication.

Competing interests. The authors declare no competing interests.

References.

1. Cancer Genome Atlas Network. Comprehensive molecular portraits of human breast tumors. *Nature* **490**, 61–70 (2012).

2. M. Zabala, N. A. Lobo, J. Antony, L. S. Heitink, G. S. Gulati, J. Lam, N. Parashurama, K. Sanchez, M. Adorno, S. S. Sikandar, A. H. Kuo, D. Qian, T. Kalisky, S. Sim, L. Li, F. M. Dirbas, G. Somlo, A. Newman, S. R. Quake, M. F. Clarke, LEFTY1 Is a Dual-SMAD Inhibitor that Promotes Mammary Progenitor Growth and Tumorigenesis. *Cell Stem Cell* **27**, 284-299.e8 (2020).

3. M. Chapellier, E. Bachelard-Cascales, X. Schmidt, F. Clément, I. Treilleux, E. Delay, A. Jammot, C. Ménétrier-Caux, G. Pochon, R. Besançon, T. Voeltzel, C. Caron de Fromentel, C. Caux, J.-Y. Blay, R. Iggo, V. Maguer-Satta, Disequilibrium of BMP2 levels in the breast stem cell niche launches epithelial transformation by overamplifying BMPR1B cell response. *Stem Cell Rep.* **4**, 239–254 (2015).

4. W.-J. Jiang, T.-H. Zhou, H.-J. Huang, L.-S. Li, H. Tan, R. Zhang, Q.-S. Wang, Y.-M. Feng, Breast Cancer Subtype–Specific Organotropism Is Dictated by FOXF2-Regulated Metastatic Dormancy and Recovery. *Cancer Res.* **85**, 644–659 (2025).

5. B. Guyot, F. Clément, Y. Drouet, X. Schmidt, S. Lefort, E. Delay, I. Treilleux, J.-P. Foy, S. Jeanpierre, E. Thomas, J. Kielbassa, L. Tonon, H. H. Zhu, P. Saintigny, W.-Q. Gao, A. de la Fouchardiere, F. Tirode, A. Viari, J.-Y. Blay, V. Maguer-Satta, An Early Neoplasia Index (ENI10), Based on Molecular Identity of CD10 Cells and Associated Stemness Biomarkers, is a Predictor of Patient Outcome in Many Cancers. *Cancer Res. Commun.* **3**, 1966–1980 (2023).

6. F. Ju, M. M. Atyah, N. Horstmann, S. Gul, R. Vago, C. J. Bruns, Y. Zhao, Q.-Z. Dong, N. Ren, Characteristics of the cancer stem cell niche and therapeutic strategies. *Stem Cell Res. Ther.* **13**, 233 (2022).

7. D. Bayik, J. D. Lathia, Cancer stem cell-immune cell crosstalk in tumour progression. *Nat. Rev. Cancer* **21**, 526–536 (2021).

8. N. Resnik, A. Erman, P. Veranič, M. E. Kreft, Triple labelling of actin filaments, intermediate filaments and microtubules for broad application in cell biology: uncovering the cytoskeletal composition in tunneling nanotubes. *Histochem. Cell Biol.* **152**, 311–317 (2019).

9. A. Rustom, R. Saffrich, I. Markovic, P. Walther, H.-H. Gerdes, Nanotubular highways for intercellular organelle transport. *Science* **303**, 1007–1010 (2004).

10. G. Hoover, S. Gilbert, O. Curley, C. Obellianne, M. T. Lin, W. Hixson, T. W. Pierce, J. F. Andrews, M. F. Alexeyev, Y. Ding, P. Bu, F. Behbod, D. Medina, J. T. Chang, G. Ayala, S. Grelet, Nerve-to-cancer transfer of mitochondria during cancer metastasis. *Nature* **644**, 252–262 (2025).

11. G. Pinto, C. Brou, C. Zurzolo, Tunneling Nanotubes: The Fuel of Tumor Progression? *Trends Cancer* **6**, 874–888 (2020).

12. M.-L. Vignais, A. Caicedo, J.-M. Brondello, C. Jorgensen, Cell Connections by Tunneling Nanotubes: Effects of Mitochondrial Trafficking on Target Cell Metabolism, Homeostasis, and Response to Therapy. *Stem Cells Int.* **2017**, 6917941 (2017).

13. L. Huang, J. Zhang, Z. Wu, L. Zhou, B. Yu, Y. Jing, D. Lin, J. Qu, Revealing the structure and organization of intercellular tunneling nanotubes (TNTs) by STORM imaging. *Nanoscale Adv.* **4**, 4258–4262 (2022).

14. I. Sáenz-de-Santa-María, J. M. Henderson, A. Pepe, C. Zurzolo, Identification and Characterization of Tunneling Nanotubes for Intercellular Trafficking. *Curr. Protoc.* **3**, e939 (2023).

15. D. Cordero Cervantes, C. Zurzolo, Peering into tunneling nanotubes-The path forward. *EMBO J.* **40**, e105789 (2021).

16. G. Pinto, I. Saenz-de-Santa-Maria, P. Chastagner, E. Perthame, C. Delmas, C. Toulas, E. Moyal-Jonathan-Cohen, C. Brou, C. Zurzolo, Patient-derived glioblastoma stem cells transfer mitochondria through tunneling nanotubes in tumor organoids. *Biochem. J.* **478**, 21–39 (2021).

17. B. Elenbaas, L. Spirio, F. Koerner, M. D. Fleming, D. B. Zimonjic, J. L. Donaher, N. C. Popescu, W. C. Hahn, R. A. Weinberg, Human breast cancer cells generated by oncogenic transformation of primary mammary epithelial cells. *Genes Dev.* **15**, 50–65 (2001).

18. G. Sapkota, C. Alarcón, F. M. Spagnoli, A. H. Brivanlou, J. Massagué, Balancing BMP signaling through integrated inputs into the Smad1 linker. *Mol. Cell* **25**, 441–454 (2007).

19. M. Inui, A. Manfrin, A. Mamidi, G. Martello, L. Morsut, S. Soligo, E. Enzo, S. Moro, S. Polo, S. Dupont, M. Cordenonsi, S. Piccolo, USP15 is a deubiquitylating enzyme for receptor-activated SMADs. *Nat. Cell Biol.* **13**, 1368–1375 (2011).

20. H.-C. Wen, A. Avivar-Valderas, M. S. Sosa, N. Girnius, E. F. Farias, R. J. Davis, J. A. Aguirre-Ghiso, p38α Signaling Induces Anoikis and Lumen Formation During Mammary Morphogenesis. *Sci. Signal.* **4**, ra34 (2011).

21. N. A. Fischbach, S. Rozenfeld, W. Shen, S. Fong, D. Chrobak, D. Ginzinger, S. C. Kogan, A. Radhakrishnan, M. M. Le Beau, C. Largman, H. J. Lawrence, HOXB6 overexpression in murine bone marrow immortalizes a myelomonocytic precursor in vitro and causes hematopoietic stem cell expansion and acute myeloid leukemia in vivo. *Blood* **105**, 1456–1466 (2005).

22. J. Ouyang, Z. Liu, X. Yuan, C. Long, X. Chen, Y. Wang, L. Liu, S. Liu, H. Liang, LncRNA PRNCR1 Promotes Breast Cancer Proliferation and Inhibits Apoptosis by Modulating microRNA-377/CCND2/MEK/MAPK Axis. *Arch. Med. Res.* **52**, 471–482 (2021).

23. M. He, Q. Jin, C. Chen, Y. Liu, X. Ye, Y. Jiang, F. Ji, H. Qian, D. Gan, S. Yue, W. Zhu, T. Chen, The miR-186-3p/EREG axis orchestrates tamoxifen resistance and aerobic glycolysis in breast cancer cells. *Oncogene* **38**, 5551–5565 (2019).

24. Y. Wang, J. Cui, X. Sun, Y. Zhang, Tunneling-nanotube development in astrocytes depends on p53 activation. *Cell Death Differ.* **18**, 732–742 (2011).

25. J. Nakhle, K. Khattar, T. Özkan, A. Boughlita, D. Abba Moussa, A. Darlix, F. Lorcy, V. Rigau, L. Bauchet, S. Gerbal-Chaloin, M. Daujat-Chavanieu, F. Bellvert, L. Turchi, T. Virolle, J.-P. Hugnot, N. Buisine, M. Galloni, V. Dardalhon, A.-M. Rodriguez, M.-L. Vignais, Mitochondria Transfer from Mesenchymal Stem Cells Confers Chemoresistance to Glioblastoma Stem Cells through Metabolic Rewiring. *Cancer Res. Commun.* **3**, 1041–1056 (2023).

26. H. Huang, D. Lu, K. Li, M. Zheng, X. Qin, X. Cui, Y. Chen, C. Chen, N. Huang, L. Zheng, J. Zhao, B. Zhu, Hsa_circ_0007031 promotes the proliferation and migration of osteosarcoma cells by sponging miR-196a-5p to regulate the HOXB6. *Biochem. Pharmacol.* **214**, 115667 (2023).

27. B. Z. Vider, A. Zimber, E. Chastre, C. Gespach, M. Halperin, P. Mashiah, A. Yaniv, A. Gazit, Deregulated expression of homeobox-containing genes, HOXB6, B8, C8, C9, and Cdx-1, in human colon cancer cell lines. *Biochem. Biophys. Res. Commun.* **272**, 513–518 (2000).

28. Z.-Y. Ding, R. Li, Q.-J. Zhang, Y. Wang, Y. Jiang, Q.-Y. Meng, Q.-L. Xi, G.-H. Wu, Prognostic role of cyclin D2/D3 in multiple human malignant neoplasms: A systematic review and meta-analysis. *Cancer Med.* **8**, 2717–2729 (2019).

29. H. Zhong, J. Yang, B. Zhang, X. Wang, L. Pei, L. Zhang, Z. Lin, Y. Wang, C. Wang, LncRNA GACAT3 predicts poor prognosis and promotes cell proliferation in breast cancer through regulation of miR-497/CCND2. *Cancer Biomark. Sect. Dis. Markers* **22**, 787–797 (2018).

30. M. C. Abba, R. Canzoneri, A. Gurruchaga, J. Lee, P. Tatineni, H. Kil, E. Lacunza, C. M. Aldaz, LINC00885 a Novel Oncogenic Long Non-Coding RNA Associated with Early Stage Breast Cancer Progression. *Int. J. Mol. Sci.* **21**, 7407 (2020).

31. T. Hirschhorn, M. Levi-Hofman, O. Danziger, N. I. Smorodinsky, M. Ehrlich, Differential molecular regulation of processing and membrane expression of Type-I BMP receptors: implications for signaling. *Cell. Mol. Life Sci. CMLS* **74**, 2645–2662 (2017).

32. J. Reindl, M. Shevtsov, G. Dollinger, S. Stangl, G. Multhoff, Membrane Hsp70-supported cell-to-cell connections via tunneling nanotubes revealed by live-cell STED nanoscopy. *Cell Stress Chaperones* **24**, 213–221 (2019).

33. V. Thayanithy, V. Babatunde, E. L. Dickson, P. Wong, S. Oh, X. Ke, A. Barlas, S. Fujisawa, Y. Romin, A. L. Moreira, R. J. Downey, C. J. Steer, S. Subramanian, K. Manova-Todorova, M. A. S. Moore, E. Lou, Tumor exosomes induce tunneling nanotubes in lipid raft-enriched regions of human mesothelioma cells. *Exp. Cell Res.* **323**, 178–188 (2014).

34. Y. C. Li, M. J. Park, S.-K. Ye, C.-W. Kim, Y.-N. Kim, Elevated levels of cholesterol-rich lipid rafts in cancer cells are correlated with apoptosis sensitivity induced by cholesterol-depleting agents. *Am. J. Pathol.* **168**, 1107–1118; quiz 1404–1405 (2006).

35. C. Gamell, N. Osses, R. Bartrons, T. Rückle, M. Camps, J. L. Rosa, F. Ventura, BMP2 induction of actin cytoskeleton reorganization and cell migration requires PI3-kinase and Cdc42 activity. *J. Cell Sci.* **121**, 3960–3970 (2008).

36. H. Ishida, K. V. Jensen, A. G. Woodman, M. E. Hyndman, H. J. Vogel, The Calcium-Dependent Switch Helix of L-Plastin Regulates Actin Bundling. *Sci. Rep.* **7**, 40662 (2017).

37. C. S. Lin, T. Park, Z. P. Chen, J. Leavitt, Human plastin genes. Comparative gene structure, chromosome location, and differential expression in normal and neoplastic cells. *J. Biol. Chem.* **268**, 2781–2792 (1993).

38. S. M. Riplinger, G. H. Wabnitz, H. Kirchgessner, B. Jahraus, F. Lasitschka, B. Schulte, G. van der Pluijm, G. van der Horst, G. J. Hämmerling, I. Nakchbandi, Y. Samstag, Metastasis of prostate cancer and melanoma cells in a preclinical in vivo mouse model is enhanced by L-plastin expression and phosphorylation. *Mol. Cancer* **13**, 10 (2014).

39. B. Janji, L. Vallar, Z. Al Tanoury, F. Bernardin, G. Vetter, E. Schaffner-Reckinger, G. Berchem, E. Friederich, S. Chouaib, The actin filament cross-linker L-plastin confers resistance to TNF-alpha in MCF-7 breast cancer cells in a phosphorylation-dependent manner. *J. Cell. Mol. Med.* **14**, 1264–1275 (2010).

40. R. A. C. Machado, D. Stojevski, S. De Landtsheer, P. Lucarelli, A. Baron, T. Sauter, E. Schaffner-Reckinger, L-plastin Ser5 phosphorylation is modulated by the PI3K/SGK pathway and promotes breast cancer cell invasiveness. *Cell Commun. Signal. CCS* **19**, 22 (2021).

41. E. Delage, D. C. Cervantes, E. Pénard, C. Schmitt, S. Syan, A. Disanza, G. Scita, C. Zurzolo, Differential identity of Filopodia and Tunneling Nanotubes revealed by the opposite functions of actin regulatory complexes. *Sci. Rep.* **6**, 39632 (2016).

42. P. J. Dawson, S. R. Wolman, L. Tait, G. H. Heppner, F. R. Miller, MCF10AT: a model for the evolution of cancer from proliferative breast disease. *Am. J. Pathol.* **148**, 313–319 (1996).

43. S.-J. Kim, S. Saeidi, N.-C. Cho, H.-B. Lee, W. Han, K. P. Kim, Y.-J. Surh, Cooperation between oncogenic NRF2 and wild-type HRAS promotes progression of breast cancer. *Cell. Signal.* **134**, 111920 (2025).

44. I. Romieu, C. Scoccianti, V. Chajès, J. de Batlle, C. Biessy, L. Dossus, L. Baglietto, F. Clavel-Chapelon, K. Overvad, A. Olsen, A. Tjønneland, R. Kaaks, A. Lukanova, H. Boeing, A. Trichopoulou, P. Lagiou, D. Trichopoulos, D. Palli, S. Sieri, R. Tumino, P. Vineis, S. Panico, H. B. A. Bueno-de-Mesquita, C. H. van Gils, P. H. Peeters, E. Lund, G. Skeie, E. Weiderpass, J. R. Quirós García, M.-D. Chirlaque, E. Ardanaz, M.-J. Sánchez, E. J. Duell, P. Amiano, S. Borgquist, E. Wirfält, G. Hallmans, I. Johansson, L. M. Nilsson, K.-T. Khaw, N. Wareham, T. J. Key, R. C. Travis, N. Murphy, P. A. Wark, P. Ferrari, E. Riboli, Alcohol intake and breast cancer in the European prospective investigation into cancer and nutrition. *Int. J. Cancer* **137**, 1921–1930 (2015).

45. C. Giampiccolo, B. Fervers, T. Coudon, D. Praud, A. Vigneron, L. Grassot, B. Mercoeur, E. Faure, P. Frenoy, M. Génard-Walton, F. Couvidat, G. Severi, F. R. Mancini, P. Roy, A. Amadou, Statistical approaches to analyse the combined effect of seven air pollutants

and breast cancer risk: a case–control study nested in the French E3N-Generations cohort. *BMC Med.* **24**, 112 (2026).

46. F. Clément, X. Xu, C. F. Donini, A. Clément, S. Omarjee, E. Delay, I. Treilleux, B. Fervers, M. Le Romancer, P. A. Cohen, V. Maguer-Satta, Long-term exposure to bisphenol A or benzo(a)pyrene alters the fate of human mammary epithelial stem cells in response to BMP2 and BMP4, by pre-activating BMP signaling. *Cell Death Differ.* **24**, 155–166 (2017).

47. O. Korenkova, S. Liu, I. Prlesi, A. Pepe, S. Albadri, F. Del Bene, C. Zurzolo, Tunneling nanotubes enable intercellular transfer in zebrafish embryos. *Dev. Cell*, S1534-5807(24)00635-X (2024).

48. Y. Perez-Riverol, Q.-W. Xu, R. Wang, J. Uszkoreit, J. Griss, A. Sanchez, F. Reisinger, A. Csordas, T. Ternent, N. Del-Toro, J. A. Dianes, M. Eisenacher, H. Hermjakob, J. A. Vizcaíno, PRIDE Inspector Toolsuite: Moving Toward a Universal Visualization Tool for Proteomics Data Standard Formats and Quality Assessment of ProteomeXchange Datasets. *Mol. Cell. Proteomics MCP* **15**, 305–317 (2016).

49. Y. Perez-Riverol, C. Bandla, D. J. Kundu, S. Kamatchinathan, J. Bai, S. Hewapathirana, N. S. John, A. Prakash, M. Walzer, S. Wang, J. A. Vizcaíno, The PRIDE database at 20 years: 2025 update. *Nucleic Acids Res.* **53**, D543–D553 (2025).

542 **Figure Legends.**

543 **Fig. 1** | Structural characterization of TNTs upon mammary cell transformation. A, Schematic
544 of our MCF10A-derived cell lines *(5)*. B, Immunofluorescence images of actin (red) in TNTs,
545 observed by Airyscan confocal microscopy with 40x oil objective. Nuclei, Hoechst labeling
546 (blue). Scale bars, 20 μm. C, TNT number (> 8 μm) quantification *per* 100 cells (left, n = 9
547 biological replicates), and % of long TNTs (> 50 μm; right, n = 4 biological replicates). Ten Z-
548 stacks of 10 sections each were taken *per* condition, and 100 cells minimum *per* experiment
549 were counted. TNTs were counted and measured in each Z-stack. Error bars depict SD. P-values
550 were calculated with one-way ANOVA with post-hoc Tukey test (ns, not significant; * $p < 0.05$;
551 ** $p < 0.01$; *** $p < 0.001$). D, Scanning electron microscopy images of TNTs of MCF10A-
552 CT, MC26 and M1B26 cells. Black arrow, TNT bulge. Scale bars MCF10A-CT: 40 and 50 μm;
553 MC26: 50 and 5 μm; M1B26: from left to right: 20, 3, 20, 3 μm. E, Transmission electron
554 microscopy images of an open-ended TNT linking two M1B26 cells, with mitochondria (red
555 asterisks). Scale bars, 5 μm (low mag), 500 nm (high mag). F, Immunofluorescence images of
556 mitochondria (green) in MCF10A-CT and M1B26 cells. Actin, red; nuclei, blue. Scale bars, 20
557 μm. G, Immunofluorescence images of actin (red) in mammary acini grown from MC26 and
558 M1B26 cells. Scale bars, 5 μm. Right, 3D-projection of a TNT linking two M1B26 cells,
559 obtained with Zeiss ZENlite3.6 software. Actin, red; nuclei, blue. H, Images of TNTs linking
560 M1B26 (GFP, green, and transmitted light) to normal human primary mammary fibroblasts
561 (transmitted light). Nuclei, blue. Scale bars, 20 μm. I, Images of TNTs linking M1B26 (GFP,
562 green) to normal human primary mammary cells. Actin, red; nuclei, blue. Asterisks: emerging
563 from M1B26 (green); between both cell types (red). Scale bars: top, 20 μm, bottom, 10 μm.

564

565 **Fig. 2** | TNTs link transformed and non-transformed mammary cells, favoring a directional
566 transfer of information. A, Fluorescence images of GFP-labeled-M1B26 (transformed - Tf;
567 green) and mCherry-labeled MCF10A (non-transformed - NoTf; red) cells, after 48 h in
568 coculture. Scale bars, 5 μm. B,C, Relative number of TNTs linking NoTf to Tf, or Tf to NoTf
569 cells (B) and TNT ratio defined as $\frac{NoTf>Tf}{NoTf-NoTf}$ (black arrows *vs* red lines) or $\frac{Tf>NoTf}{Tf-Tf}$ (black
570 arrows *vs* green lines) after 48h in coculture (C). Z stacks of 10 sections each were taken *per*
571 condition and 100 cells minimum were counted. TNTs were counted and measured in each Z-
572 stack. Error bars depict SD. Statistical significance was calculated using an unpaired Student's
573 two-sided t test with Welch's correction (n = 5 biological replicates; *** $p < 0.001$). D,

574 Fluorescence images of material transfer (green dots) from Tf (green) to NoTf cells.
575 Membranes, red; nuclei, blue. Scale bars: 100 μm, in zoom 20 μm. E, Time-lapse snapshots of
576 green material trafficking within a TNT bulge (*), from a (green) Tf to NoTf cells after 48 h in
577 coculture. Membranes, red; nuclei, blue. Scale bar, 100 μm; images recorded for 75 min, with
578 one image every 18 min (see Supplementary Movie 1). F, Flow cytometry analysis of an 8-day
579 coculture of green Tf and red NoTf cells, with a schematic of NoTf accepting material from Tf
580 cells (top: NoTf accept green, red cell with green dots), and Tf cells accepting material from
581 NoTf cells (bottom: Tf accept red, green cell with red dots). G,H, Quantification of the
582 percentage of exchange (G; n = 8 biological replicates) and fluorescence intensity (H; n = 7
583 biological replicates), for indicated transfer. Error bars depict SD. Statistical significance was
584 calculated using an unpaired Student's two-sided t test with Welch's correction (*** $p < 0.001$).
585 I, Schematic of the experimental design of coculture experiments. J,K, Quantification of the
586 number of acceptor cells *per* 10,000 cells (J), and fluorescence intensity (K), in standard or
587 Transwell™ cocultures, for indicated transfer involving normal human primary mammary
588 (normal) and M1B26 cells (Tf). Error bars depict SD. Statistical significance was calculated
589 using an unpaired Student's two-sided t test with Welch's correction (n = 3 biological replicates;
590 ns, not significant; * $p < 0.05$; ** $p < 0.01$).

591

592 **Fig. 3** | TNT-dependent phenotypic changes of non-transformed cells acceptor of material from
593 transformed cells. A, Schematic of the experimental design: 4 cell populations, sorted by flow
594 cytometry (NoTf, Tf, NoTf in coculture without fluorescent transfer [non-transformed non-
595 acceptor cells - NoTf no accept], NoTf in coculture with fluorescent transfer [non-transformed
596 acceptor cells - NoTf accept]), underwent proteomic analyses and RT-qPCR. B,C, Volcano plot
597 (B) showing Log_2 enrichment of individual proteins in NoTf accept compared to NoTf no
598 accept cells from the same coculture (see schematic). P-value threshold was set at 0.05 and 0.8
599 for Log_2 fold change. C, To obtain a larger pool of hits, it was lowered to 0.5, generating a list
600 of 193 proteins upregulated in NoTf accept cells, used to generate the GOBP subset with
601 STRING (https://string-db.org). D,E, Box and whiskers plots of Log_2LFQ values (Protein
602 Levels) of EST1 (*CES1*), Plastin-2 (*LCP1*), Rab-6B (*RAB6B*), TRIQK (*TRIQK*) (D), and H-
603 Ras and K-Ras (E), for indicated sorted cell populations. Statistical significance was calculated
604 using one-way ANOVA with Dunnett's multiple comparison test (n = 5 biological replicates; *
605 $p < 0.05$; ** $p < 0.01$; *** $p < 0.001$; **** $p < 0.0001$). For clarity, comparisons with Tf cells
606 were omitted, and in (E), only significant comparison are shown. F,G, Immunofluorescence

607 images of actin (red) and tubulin (green) in (F) HMLE and HMLER cells, and (G) MCF10A,
608 MCF10.AT1 and MCF10.DCIS cells. Nuclei, blue. Scale bars = 20 µm. H,I, From left to right:
609 quantification of TNT number *per* cell, average length, and percentage of long TNTs in
610 indicated cell lines. Ten Z-stacks of 10 sections each were taken *per* condition and 100 cells
611 minimum *per* experiment were counted. TNTs were counted and measured in each Z-stack.
612 Statistical significance was calculated using an unpaired Student's two-sided t test with Welch's
613 correction (n = 8 and n = 5 biological replicates for HMEC-derived and MCF10A-derived cell
614 lines, respectively; ns, not significant; ** $p < 0.01$).

615

616 **Fig. 4** | Expression of actors of the BMP signaling pathway is enhanced in acceptor cells after
617 TNT transfer. A, Box and whiskers plots of Log_2LFQ values (Protein Levels) of ID1, Nup214,
618 Spartin, USP15, ATF2, MAPKAPK2 and Rac1, for indicated sorted cell populations. Statistical
619 significance was calculated using one-way ANOVA with Dunnett's multiple comparison test (n
620 = 5 biological replicates; * $p < 0.05$; ** $p < 0.01$; *** $p < 0.001$; **** $p < 0.0001$). For clarity,
621 only comparison between NoTf and NoTf accept cells is shown. B, Immunofluorescence
622 images of actin (red) and BMPR1b (green) in indicated cells. Nuclei (blue). Scale bars, 20 µm.
623 C, Correlative light scanning electron microscopy (SEM) of BMPR1b, immunostained with
624 Alexa Fluor®488-Fluoronanogold™ (green) in M1B26 cells. From left to right: confocal,
625 scanning electron microscopy, zooms, correlative (overlay). Scale bars, 10 µm, unless
626 otherwise indicated. D, Immunofluorescence of actin (green), after transfection with siRNA
627 pools targeting *BMPR1b* (siBMPR1b) or *GPER* (siGPER). Non-targeting siRNA: siCTRL. E,
628 *BMPR1B* and *GPER* transcript and protein expression upon their silencing (top),with siCTRL
629 set at 1 (n = 4), and (bottom) TNT number (> 8 µm) *per* cell and % of long TNTs (> 50 µm)
630 upon indicated silencing, normalized against siCTRL. Error bars depict SD. Statistical
631 significance was calculated using an unpaired Student's two-sided t test with Welch's correction
632 (n = 4 biological replicates, *** $p < 0.001$). F, Schematic of experimental design: after sorting,
633 cell populations were either lysed and subjected to RT-qPCR for selected transcript analyses, or
634 grown for several weeks with or without BMP2/IL6, and immunoblot analyses performed at
635 end points. G, RT-qPCR measurement of BMPR1b mRNA in indicated cell populations, the
636 expression in NoTf cells (monocultures) set at 1. Statistical significance was calculated using
637 one-way ANOVA with post-hoc Tukey test (n = 5 biological replicates). For clarity, only
638 comparison between NoTf accept and NoTf cells is shown (**** $p < 0.0001$).

Fig. 5 | Non-transformed cells acceptor of information from transformed cells *via* TNTs display preneoplastic features. A, Left, quantification of BMPR1b immunoblots performed on NoTf accept cells grown in the presence of BMP2/IL6, for indicated weeks post sorting. Box and whiskers plot of 6 biological replicates. Statistical significance was calculated using a one-way ANOVA with non-parametric Kruskal-Wallis test, and for clarity, only p-values ≤ 0.05 are indicated. Right, quantification of BMPR1b immunoblots performed on indicated cells, 14 weeks post sorting, with NoTf conditions set at 1 (n = 6 biological replicates). Statistical significance was calculated using a one-way ANOVA with post-hoc Tukey test (*** $p < 0.001$). B,C, Quantification of p-SMAD1/5/8 / SMAD1/5/8 (B) and p-p38/p38 (C) immunoblots performed on NoTf accept cells grown in the presence of BMP2/IL6, for indicated weeks post sorting. Box and whiskers plot of 6 biological replicates. Statistical significance was calculated using a one-way ANOVA with non-parametric Kruskal-Wallis test, and for clarity, only p-values ≤ 0.05 are indicated. D, RNA-sequencing results of transcriptomic expression levels of *HOXB6, CCND2, EREG* and *HRAS* in indicated cell lines (n = 3 biological replicates). Data deposited on the Gene Expression Omnibus repository, GSE186734 *(5)*. Error bars depict SD. Statistical significance was calculated using a one-way ANOVA with post-hoc Tukey test (* $p < 0.05$; ** $p < 0.01$; *** $p < 0.001$; **** $p < 0.0001$). E, RT-qPCR measurements of HOXB6, CCND2, EREG and HRAS mRNA in indicated cell populations, with the expression in NoTf cells set at to 1. Error bars depict SD. Statistical significance was calculated using a one-way ANOVA with post-hoc Tukey test (biological replicates: n = 8 for *HOXB6*, n = 5 for *CCND2*, n = 7 for *EREG*, n = 8 for *HRAS*). For clarity, only comparisons between NoTf, NoTf Transwell and NoTf accept cells are shown (* $p < 0.05$; ** $p < 0.01$; *** $p < 0.001$; **** $p < 0.0001$). F, Quantification of soft agar clones of indicated sorted cells, after 8, 10, 14 and 16 weeks in culture with or without BMP2/IL6 (n = 3 biological replicates). Error bars represent SD. Statistical significance was calculated using a one-way Welch and Brown-Forsythe ANOVA test (* $p < 0.05$; ** $p < 0.01$; *** $p < 0.001$; **** $p < 0.0001$). For clarity, only p-values ≤ 0.05 are indicated, and comparisons with Tf cells are omitted. G, Model depicting how TNTs might be involved in the propagation of a BMP-dependent preneoplastic state. Fibrils and fibers depict extracellular matrix components.

Cuella Martin *et al* Figure 1

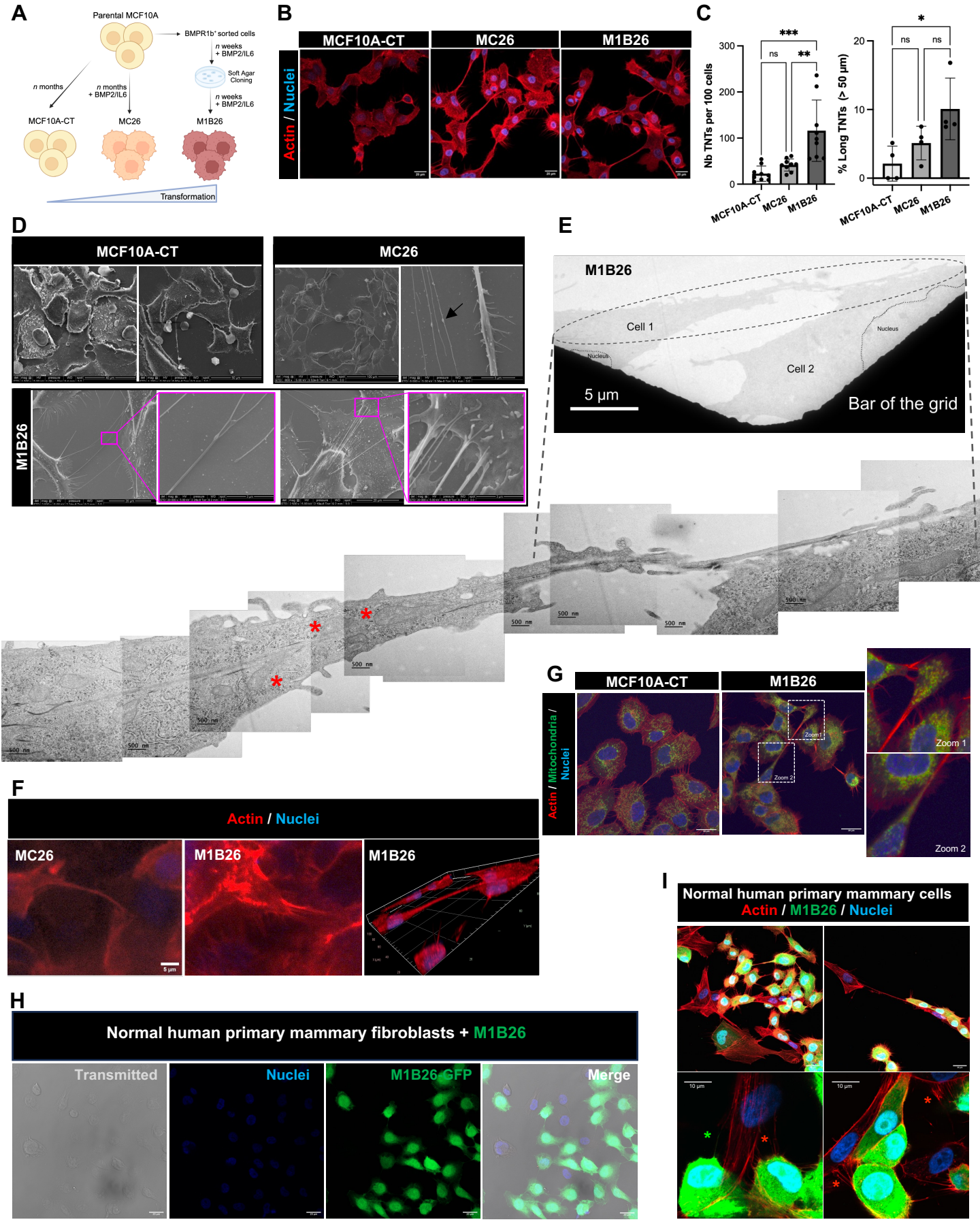

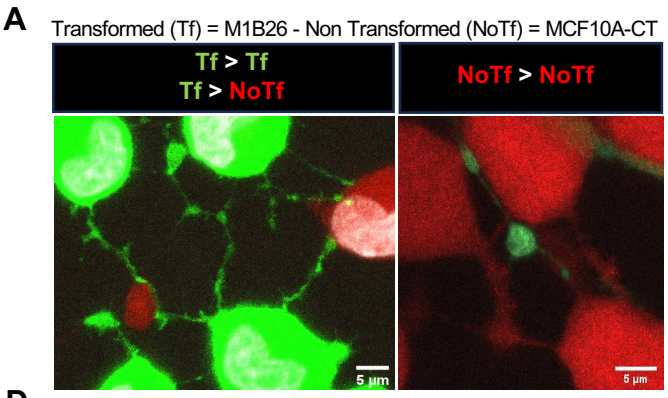

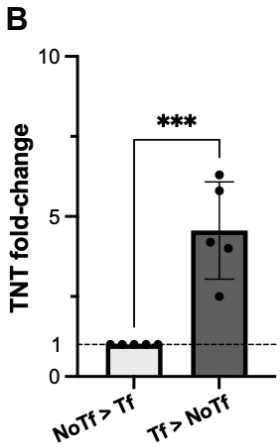

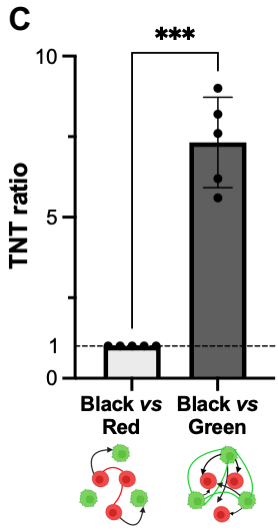

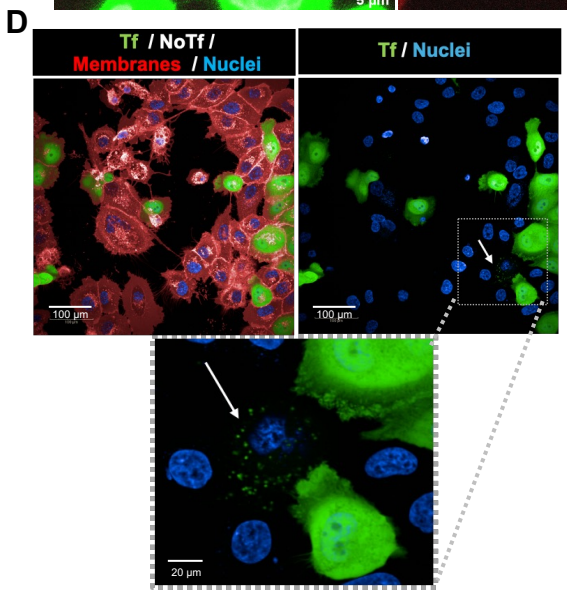

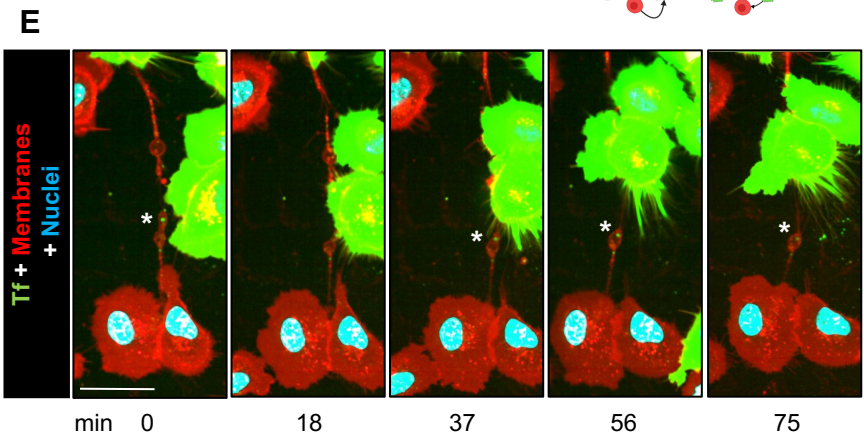

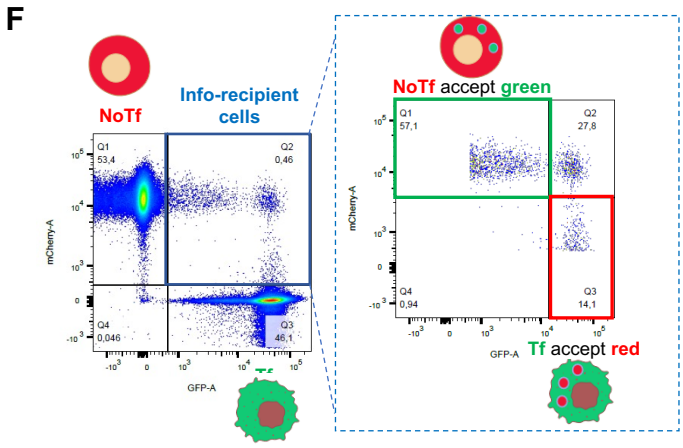

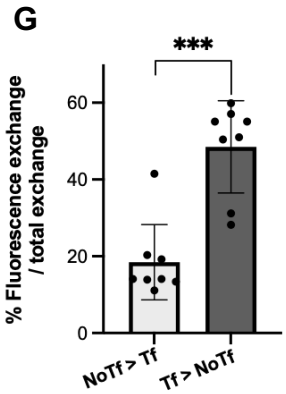

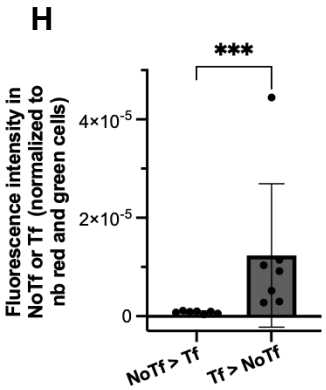

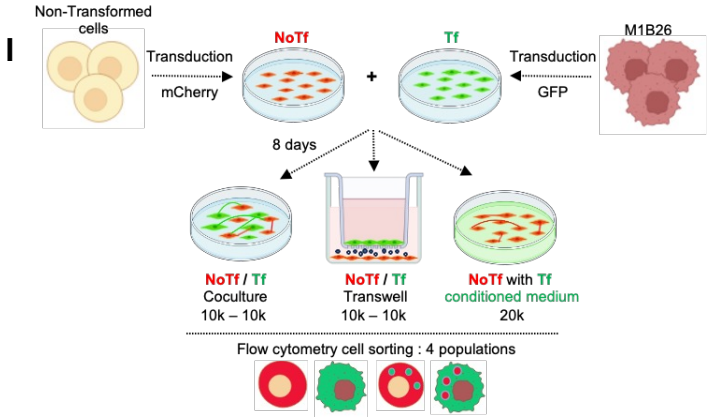

NoTf = Normal human primary mammary cells

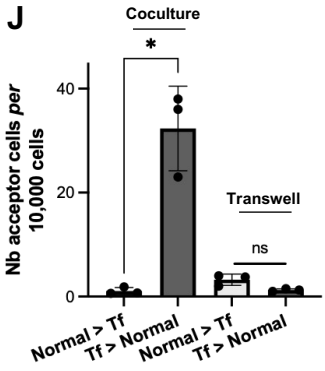

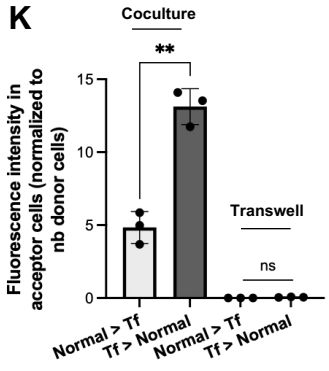

Cuella Martin *et al* Figure 3

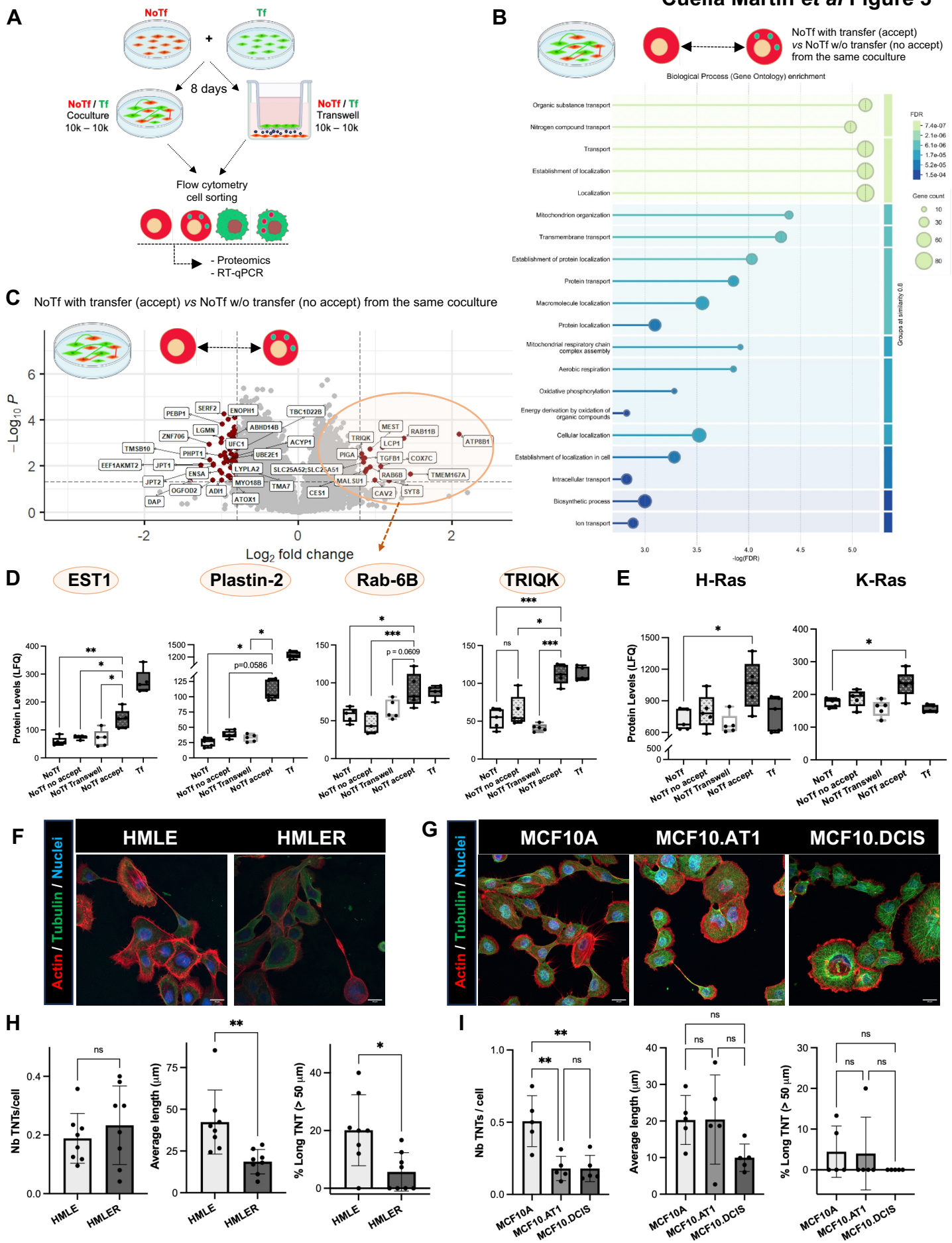

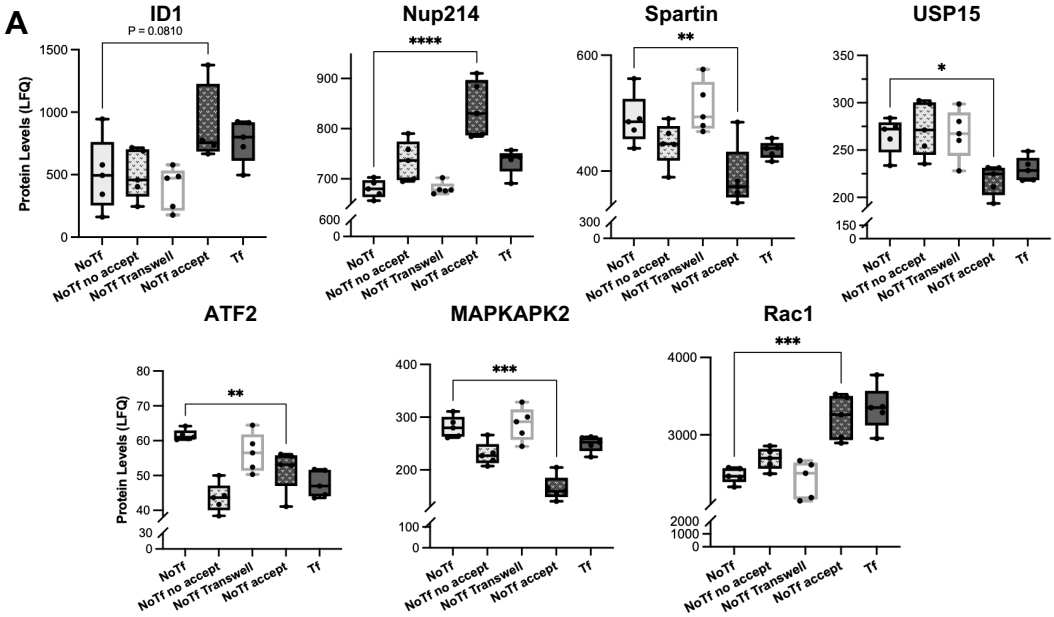
A
ID1
P = 0.0810
Nup214
****
Spartin
**
USP15
*
ATF2
**
MAPKAPK2
***
Rac1
***
Protein Levels (LFQ)
NoTf
NoTf no accept
NoTf Transwell
NoTf accept
Tf

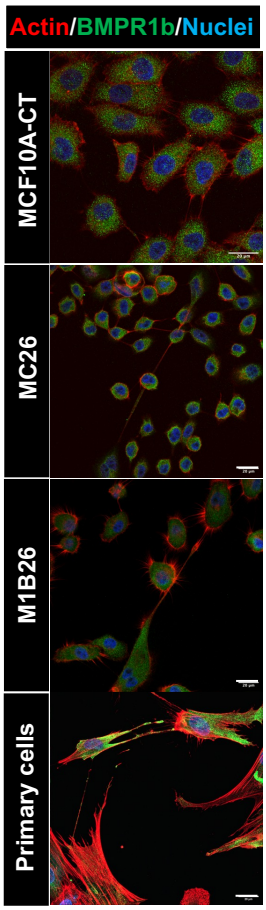
B
Actin/BMPR1b/Nuclei
MCF10A-CT
MC26
M1B26
Primary cells

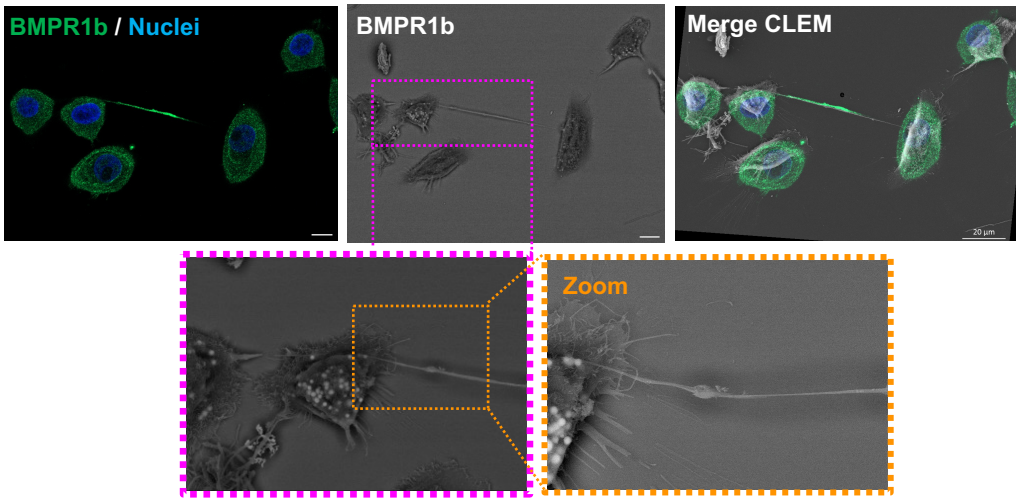
C
BMPR1b / Nuclei
BMPR1b
Merge CLEM
Zoom

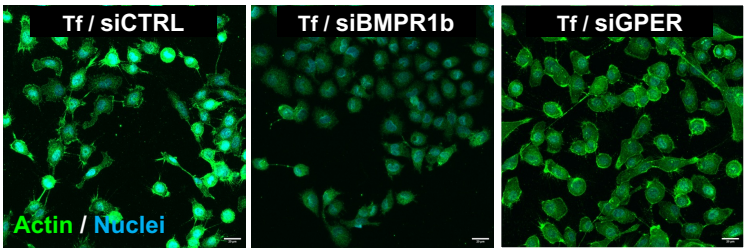
D
Tf / siCTRL
Tf / siBMPR1b
Tf / siGPER
Actin / Nuclei

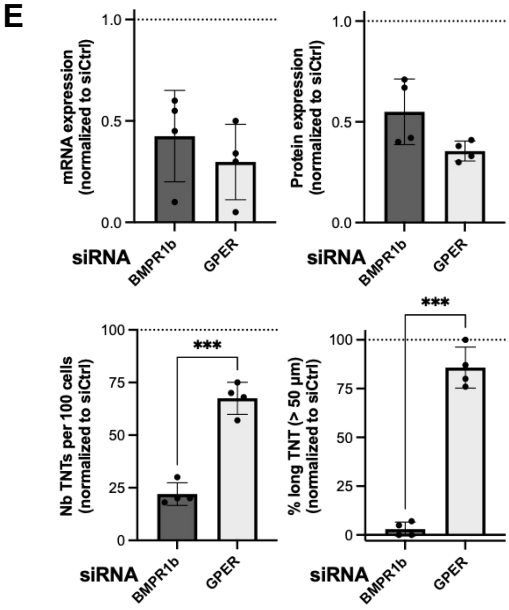
E
mRNA expression (normalized to siCtrl)
Protein expression (normalized to siCtrl)
Nb TNTs per 100 cells (normalized to siCtrl)
% long TNT (> 50 µm) (normalized to siCtrl)
siRNA
BMPR1b
GPER
***

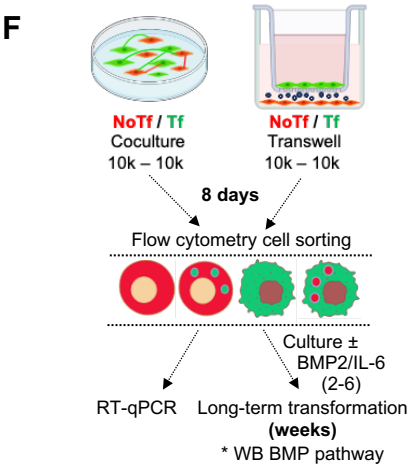
F
NoTf / Tf
Coculture
10k – 10k
NoTf / Tf
Transwell
10k – 10k
8 days
Flow cytometry cell sorting
Culture ±
BMP2/IL-6
(2-6)
RT-qPCR
Long-term transformation
(weeks)
* WB BMP pathway

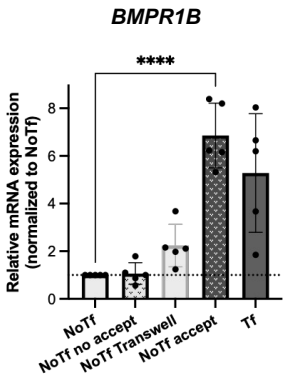
G
BMPR1B
****
Relative mRNA expression (normalized to NoTf)
NoTf
NoTf no accept
NoTf Transwell
NoTf accept
Tf

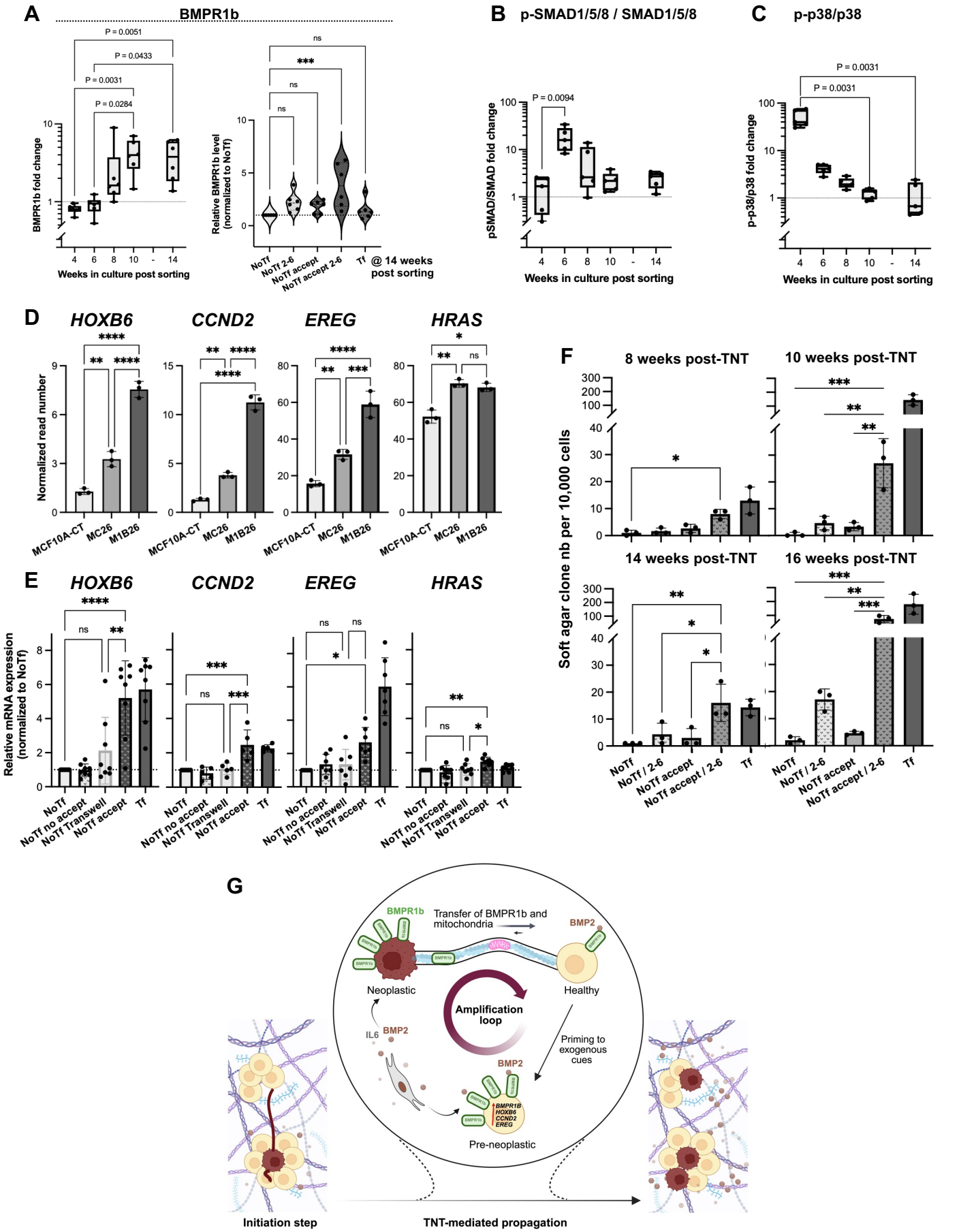
A
BMPR1b
P = 0.0051
P = 0.0433
P = 0.0031
P = 0.0284
BMPR1b fold change
Weeks in culture post sorting
ns
***
ns
ns
Relative BMPR1b level (normalized to NoTf)
NoTf
NoTf 2-6
NoTf accept
NoTf accept 2-6
Tf
@ 14 weeks post sorting
B
p-SMAD1/5/8 / SMAD1/5/8
P = 0.0094
pSMAD/SMAD fold change
Weeks in culture post sorting
C
p-p38/p38
P = 0.0031
P = 0.0031
p-p38/p38 fold change
Weeks in culture post sorting
D
HOXB6
CCND2
EREG
HRAS
Normalized read number
MCF10A-CT
MC26
M1B26
E
HOXB6
CCND2
EREG
HRAS
Relative mRNA expression (normalized to NoTf)
NoTf
NoTf no accept
NoTf Transwell
NoTf accept
Tf
F
8 weeks post-TNT
10 weeks post-TNT
14 weeks post-TNT
16 weeks post-TNT
Soft agar clone nb per 10,000 cells
NoTf
NoTf / 2-6
NoTf accept
NoTf accept / 2-6
Tf
G
BMPR1b
Transfer of BMPR1b and mitochondria
BMP2
Neoplastic
Healthy
Amplification loop
IL6
BMP2
Priming to exogenous cues
BMP2
BMPR1B
HOXB6
CCND2
EREG
Pre-neoplastic
Initiation step
TNT-mediated propagation

Supplementary materials & methods to :

Tunneling nanotubes propagate a BMP-dependent preneoplastic state.

Cristina Cuella Martin[1,2,3], Thanh Thuy Nguyen * [1,2,3], Alexia Bertin * [1,2,3], Kevin Geistlich[1,2,3,4], Boris Guyot[1,2,3], Sylvain Lefort[1,2,3], Emmanuel Delay[1,2,3,4], Charline Dalverny[3,5], Alice Boissard[6], Cécile Henry[6], François Guillonneau[6,7,8], Eve-Isabelle Pécheur §* [1,2,3] and Véronique Maguer-Satta §* [1,2,3,4]

1, CNRS UMR5286, Centre de Recherche en Cancérologie de Lyon, 69008 Lyon, France;
2, Inserm U1052, Centre de Recherche en Cancérologie de Lyon, 69008 Lyon, France;
3, Université Claude Bernard Lyon 1, Lyon, France;
4, Centre Léon Bérard, 69008 Lyon, France;
5, Centre Technologique des Microstructures (CTμ), 69622 Villeurbanne, France;
6, Prot'ICO proteomics facility, Institut de Cancérologie de l'Ouest, 49055 Angers, France,
7, Nantes Université, Inserm, CNRS, CRCI2NA, U1307, UMR6075, 44000 Nantes, France;
8, Equipe Labellisée Ligue Contre le Cancer, Paris, France.

* These authors contributed equally; § Co-corresponding authors

26 **Materials & Methods.**

27 ***Cell lines.*** MCF10A cells were purchased from ATCC (ATCC Batch#7635052). The MC26 cell
28 line was obtained upon MCF10A chronic exposure to BMP2 and IL6, while M1B26 came from
29 MCF10A first sorted on BMPR1b overexpression, then chronically exposed to BMP2 and IL6,
30 and derived from a soft agar colony (*1*). MCF10A, MCF10A.DCIS, MC26 and M1B26 were
31 cultured in phenol-red free Dulbecco's Modified Eagle Medium Ham's F12 (DMEM-F12,
32 Gibco), supplemented with 2% horse serum (Gibco), 10,000 U/ml - penicillin and 10,000 µg/ml
33 - streptomycin (Gibco) (P/S), 10 µg/ml insulin (NovoRapid CLB pharmacy), 0.5 µg/ml
34 hydrocortisone (Sigma), 100 ng/ml cholera toxin (Sigma), 20 ng/ml epithelial growth factor
35 (Sigma). MCF10A.AT1 and MCF10A.DCIS, obtained from ATCC, were cultured with the
36 same medium supplemented with 5% horse serum. MC26 and M1B26 culture medium was
37 supplemented with 5 ng/ml BMP2 (R&D) and 10 ng/ml IL6 (Peprotech). HMEC cells were
38 obtained from R. Weinberg's group (MIT, Massachussetts, USA). Cells were grown in 1:1
39 MEGM Complete Medium [Lonza/Clonetics, CC-3150] plus DMEM/F12 (1:1) with
40 supplements : 10 ng/ml hEGF, 0.5 µg/ml hydrocortisone, 10 µg/ml insulin, 10,000 U/ml -
41 penicillin and 10,000 µg/ml - streptomycin (Gibco). Cells were passed twice a week at 70% of
42 confluence. Cells washed twice with Phosphate Buffer Saline (PBS, Life Technologies) were
43 treated with 0.48 mM Versene (ThermoFischer, #15040066) for 20 min, or with trypsin 0.05%
44 for 10 min at 37°C. After collecting cells, neutralization was achieved with PBS/20% FBS.
45 Plated cells were incubated at 37°C under 5% atmospheric CO_2.

46

47 ***Fluorescent cell lines generation.*** Fluorescent cells were obtained by viral transduction of
48 parental ones with lentivirus produced in 293T cells by transfection of three plasmids encoding
49 respectively for the viral envelope G of VSV (vesicular stomatitis virus), the structural and
50 enzymatic proteins Gag and Pol of the lentivirus, and for a reporter gene mCherry or GFP (in
51 collaboration with AniRA lentivectors production facility from the CELPHEDIA Infrastructure
52 and SFR Biosciences, UAR3444/CNRS, US8/Inserm, ENS de Lyon/UCBL). Of note, these
53 viruses are defective, meaning that no viral protein or particle are produced by cells after
54 transduction.

55

56 ***Coculture of MCF10A-CT and M1B26 cells.*** Cells were cocultured at a 50% ratio for up to 8
57 days in MCF10A complete medium. Fresh medium was added every 3-4 days. For the
58 conditioned medium assay, the M1B26 green or MCF10A-CT green supernatant was collected,
59 centrifuged for 5 min at 800xg, and filtered on a 20 µm-pore filter. Monocultures of fluorescent

cells were grown for 8 days in this medium, and fresh one was added after 3-4 days. For cocultures in Transwell, a Transwell system with pores of 0.4 µm was used (Merck Millipore, #PHP01250). Four and ½ ml of MCF10A complete medium was added at the bottom, and 450 µl of MCF10A complete medium at the top of the insert. Cells were cocultured in the Transwell system for 8 days, and fresh complete medium was added after 3-4 days.

Acini formation. The protocol for 3D-acini formation was derived from Vidi *et al* (*2*), using the 3D-embedded culture process.

Gene silencing with siRNA. Silencing of BMPR1b and GPER was performed using small interfering RNAs, purchased at Horizon Discovery (ON-TARGETplus siRNA, SMARTpool siRNA). Cells were transfected through electroporation by a Neon Electroporator Device.

Western-Blotting. Cells were harvested, pelleted, and lysed in CHAPS buffer (40 mM Hepes pH 7.4, 120 mM NaCl, 2 mM EDTA, 0.3% CHAPS) and protease/phosphatase inhibitors (Roche Complete inhibitor cocktail #4693132001). Proteins were then assayed by spectrophotometry, along with a BSA standard curve, using the Pierce™ Coomassie Protein Assay Kit (Thermo Fisher Scientific). Twenty to 30 µg of proteins were used and mixed with 1X Laëmmli and H_2O, and samples boiled for 5 min at 95°C. The mixture was loaded onto 10% acrylamide gels, and run in 25 mM Tris, 192 mM glycine, 0.1% SDS. After transfer onto PVDF membranes previously activated in ethanol and transfer buffer (Biorad™ Transfer buffer, 20 % ethanol) using the Transblot Turbo^{TM} from BioRad. Membranes were then incubated for 1h with TBST [Tris-buffered saline 1X (Euromedex) containing 0.1% Tween-20] with 5% fat-free BSA for membrane saturation at room temperature. Primary antibodies were incubated at 4°C overnight. Primary antibodies used were directed against BMPR1b (1:300 Abcam, ab78417 and 1:300 Santa Cruz, sc-515886), GAPDH (1:10,000 Cell Signaling Technology, #8884 and 1:50,000, Proteintech #600004-1), p-SMAD1/5/8 (1:500, Cell signalling, #13820), Smad1/5/8 (1:500, Santa Cruz, sc-6031-R), p-ERK (1:2,000, Cell Signalling Technology, #4370S), ERK (1:1,500, Cell Signalling Technology #4695S), p-p38 (1:2,000, BD Bioscience #612288), p38 (1:2,000, BD Biosciences, #612168), GPER (1:500 Novus Biologicals, #NLS4290 or 1:500, Invitrogen, #PA5-28647), EREG (1:400, abcam, #1041688-1), Cyclin-D2 (1:3,000, Proteintech, #67048-i-IG), or HoxB6 (1:1,500, Santa Cruz, sc-166950), in 5% BSA. After TBST buffer washes, membranes were incubated at room temperature for 1h with horseradish peroxydase (HRP)-conjugated secondary antibodies goat anti-rabbit, goat anti-mouse or rabbit

anti-goat secondary antibodies (Jackson, #111-035-003, #115-035-003, #305-035-003) at 1:10,000 in TBST/3% BSA. After extensive washings with TBST buffer, revelation was achieved through Clarity™ Western ECL Substrate (Biorad) and Chemidoc™ Imaging System (Biorad). Protein bands were quantified using the ImageLab™ software.

Immunofluorescence. Cells were seeded on coverslips and grown at 60% of confluence. For staining BMPR1b and actin staining, the following protocol was used : after washing with PBS, fixation was performed for 20 min in 4% final paraformaldehyde (PFA) at room temperature (RT). After PBS washing, permeabilization and saturation were performed for 45 min with PBS/3% BSA/0.3% Triton X-100 at RT. After PBS washing, primary antibody against BMPR1b (1:300 #sc-293428 Santa Cruz) and its corresponding isotype were incubated overnight at 4°C. Coverslips were washed three times with PBS/3% BSA/0.1% Tween-20 for 10 min. Secondary antibody goat anti-mouse Dylight 488 diluted 1:1,000 was incubated for 45 minutes at RT, with 1:50,000 of Hoechst 33342 (Invitrogen #H3570) and Phalloidin AlexaFluor-Plus 647 (Invitrogen, #A30107). Then, cells were washed twice with PBS/3% BSA/0.1% Tween-20 for 5 minutes and twice with PBS for 5 minutes. Coverslips were then mounted using the Dako mounting medium (Agilent, ref S3023). For mitochondria staining, MitoTracker™ deep red or green were used (Thermofischer, #M22426 or #M7514, respectively). Microscopic observations were performed using the x40 oil immersion objective of a confocal Zeiss LSM980 microscope, with Airyscan mode. This was done at the LYMIC-PLATIM, Imaging and Microscopy Core Facility of SFR Biosciences (UMS3444), Lyon, France. Images were taken in 16-bit, and formatted via the Fiji software. For immunofluorescence staining of actin (Phalloidin) and tubulin, the following protocol optimized by the Dr. C. Zurzolo's team was used to identify and characterize TNTs. Subconfluent cells were fixed for 15min at RT, with a 4% PFA/0.05% glutaraldehyde mixture in PBS. The fixation buffer was removed, and and cells incubated with 100 mM NH_4Cl for 10min at RT to quench the PFA-related autofluorescence. After PBS washing, cells were saturated with 2% BSA for 20 min at RT. The primary antibody against tubulin was diluted at 1:500 (Abcam #ab6046) in 2% BSA, and incubated for 1h at RT, or OVN at 4°C. After PBS washing, cells were incubated with a secondary goat anti-rabbit antibody-488nm, diluted at 1:1,000 in 2% BSA, and incubated for 40 min in the dark at RT. After PBS washing, cells were finally incubated with phalloidin AlexaFluor Plus-647 (Invitrogen, #A30107) diluted at 1:1,000, and with Hoechst 33342 (Invitrogen, #H3570), diluted at 1:50,000 in 1% BSA, for 30 min in the dark. After PBS washing, slides were mounted using the Dako mounting medium (Agilent, S3023). Microscopic observations were performed

128 with the objective 40x oil of a confocal Zeiss LSM980 microscope, with Airyscan mode. This
129 was performed at the LYMIC-PLATIM, Imaging and Microscopy Core Facility of SFR
130 Biosciences (UMS3444), Lyon, France, and at the imaging quantitative center of Lyon Est
131 (CIQLE). Images were taken in 16-bit, and formatted *via* the Fiji software. TNTs were finally
132 manually counted with the Fiji software.
133
134 ***Live imaging.*** Live imaging was performed after 48h of coculture in µslide 8-well plate with
135 thin glass bottom (Ibidi, #80827), adequate for imaging. After PBS washing, cells were stained
136 with Cell Mask Deep Red (at 1:500, #C10046, Invitrogen) and Hoechst (Invitrogen, #H3570,
137 1:500), diluted in complete medium, for 10 min at 37ºC. After PBS washing, complete fresh
138 medium was added. Observations were performed using the Opera Phenix HCS microscope
139 with the 40x water immersion objective.
140
141 ***RT-qPCR.*** For RT-qPCR analyses, pelleted cells were resuspended with 300µl Trizol reagent
142 (Life Technologies^{TM}). Total RNA purification was achieved using direct-zol RNA MicroPrep
143 w/ Zymo-Spin IC Columns extraction kit (Ozyme). For sorted fluorescent cells after coculture,
144 RNA extraction was performed using the AllPrep DNA/RNA Micro Kit (Qiagen, #80284). C-
145 DNA was then obtained using PrimeScript™ RT Reagent Kit (Takara kit), and qPCR then
146 performed using the SyberGreen Premix Ex Taq™ (Takara kit) as the fluorescent DNA
147 intercalant, and amplicons read by a Light Cycle 480 (Roche, LC480). Results were normalized
148 to housekeeping genes : TATA-binding protein (*TBP*) and hypoxanthineguanine phosphoribosyl
149 transferase (*HPRT*) (see Table S4 for primers used). An additional normalization to control cells
150 (MCF10A or MCF10A-CT) was also performed.
151
152 ***Proteomic analyses.*** *Sample preparation for proteome analysis*. Proteome analyses were
153 performed at the Prot'ICO proteomics facility: FACS-sorted samples (FACS-Melody) were
154 quickly thawed and proteins equivalent to 66,000 cells were concomitantly extracted and
155 denatured while thiol groups were chemically reduced in 46 µl 5% SDS, containing 5 mM
156 TCEP, 10 mM chloroacetamide, heated in a thermostatic shaker set at 95°C under 500xg for 30
157 min. Sonication was performed twice 30s using an ultrasonic sonicator bath (ThermoFisher
158 Scientific). S-Trap Micro Spin Column was used according to the manufacturer's protocol
159 (Protifi, Farmingdale, NY, USA), to trap precipitated proteins under acidic and hydrophobic
160 conditions to remove detergents, and 1µg of porcine trypsin (Sciex) was used at 37°C overnight
161 to cleave peptide bonds at carbonyl-side of lysine and arginine to generate bottom-up LC MS-

compatible peptides. Resulting peptides were then cleared from potential insoluble material by centrifugation. Peptides were then speed-vacuum dried and resuspended in 0.1% formic acid (FA) before injection in LC-MS/MS with DIA-PASEF mode using a TIMS-TOF Pro 2 mass spectrometer (Bruker, Bremen, Germany).

LC-MS/MS setup. Each sample was loaded and separated on a C18 reverse phase column (Aurora Ultimate series 1.7µm particles size, 75µm inner diameter and 25cm length, IonOptics, Fitzroy, Australia) using a NanoElute 2 LC system with Hystar 6.3.1.8 software (Bruker, Bremen, Germany). Eluates were electrosprayed for a 60 min-long duration of the hydrophobicity gradient ranging from 99% of solvent A containing 0.1% FA in milliQ-grade H_2O, to 27% of solvent B containing 80% acetonitrile containing 0.1% FA in mQ-H_2O. The mass spectrometer acquired data throughout the elution process and operated in data-independent analysis (DIA) with PASEF-enabled method, using the TIMS-Control software v.5.1.8 (Bruker). Samples were injected in batch replicates in order to circumvent possible interferences of technical biases. The m/z acquisition range was 250–1201 with an ion mobility range of 0.7–1.25 1/*K*0 [V s/cm^2], which corresponded to an estimated cycle time of one second. DIA-PASEF windows, and collision energy were also left to default with a base of 0.85 1/*K*0 [V s/cm^2] set at 20 eV and 1.30 1/*K*0 [V s/cm^2] set at 59 eV. TOF mass calibration and TIMS ion mobility 1/*K*0 were performed linearly using three reference ions at 622, 922, and 1,222 m/z (Agilent Technology, Santa Clara, CA, USA)

LC-MS/MS raw data analysis. The raw data were extracted, normalized and analyzed using Spectronaut® 19.0.24 (Biognosys A.G. Schlieren, Switzerland) in DirectDIA+ mode, which modelized elution behavior, mobility and MS/MS events based on the "Uniprot/SwissprotKB model organism_9606_2024_04_03" FASTA sequence database of 45,514 human proteins and 381 entries of common contaminant proteins. Protein identification false discovery rate (FDR) was restricted to 1% maximum, and inter-injection data normalization. The enzyme's cleavage specificity was that of trypsin. The precursor and fragment mass tolerances were set to default. Acetyl (protein N-term) and oxidation of methionines were set as variable modifications, while thiol groups from cysteines were considered completely alkylated by carbamidomethylation. A minimum of two ratios of peptides was required for relative quantification between groups. Protein quantification analysis was performed using Label-Free Quantification (LFQ) intensities. Spectronaut also linked Gene Ontology terms to identified protein using the EBI GO database, and its statistical tools were used to visualize data, assess reproducibility and quality to allow quantitative dataset comparisons. The mass spectrometry proteomics data have

been deposited to the ProteomeXchange Consortium via the PRIDE (*3*, *4*) partner repository with the dataset identifier PXD060023.

Volcano plots were generated with the package EnhancedVolcano (https://bioconductor.org/packages/release/bioc/html/EnhancedVolcano.html), with a p-value threshold set at 0.05 and a LogFC threshold set at either 0.8 or 0.95. Pathway analysis were performed using STRING (https://string-db.org/) with the Biological Process category from the Gene Ontology collection. For the search of BMP and P38 pathways targets, a combination of several pathways from different collections have been compiled (GOBP_POSITIVE_REGULATION_OF_BMP_SIGNALING_PATHWAY ; GOBP_REGULATION_OF_BMP_SIGNALING_PATHWAY ; GOBP_RESPONSE_TO_BMP ; PID_BMP_PATHWAY ; BIOCARTA_P38MAPK_PATHWAY ; GOBP_P38MAPK_CASCADE ; GOBP_REGULATION_OF_P38MAPK_CASCADE ; REACTOME_P38MAPK_EVENTS ; WP_P38_MAPK_SIGNALING).

Flow cytometry and cell sorting. After cell detachment as previously described, cells were resuspended in PBS/1% FBS. Sorting of cocultured cells was performed using the BD FACSMelody™ Cell Sorter, at the CRCL Flow cytometry platform, SFR Lyon-EST (CYLE). Results were analyzed with the FlowJo™ software.

Soft agar colony formation assay. Each well of a 6-well plate was coated with agarose 1.5% mixed with 2X complete medium. After polymerisation at RT, a top layer was added, containing agarose 0.9%, mixed with 2X complete medium containing 13,000 cells. PBS was added between wells, so that the agar would not dry out. Clone counting was performed manually after 3-4 weeks.

Electron microscopies. *Transmission EM.* Cell samples in Petri dishes were washed 3 times 15min in sodium cacodylate buffer 0.2M pH 7.3, and fixed for 1h in glutaraldehyde 2% in the same buffer at 0.1M. After washing in buffer, samples were prepared for TEM observations after Epoxy resin embedding and microtome ultrathin sectioning at the Center for Microstructure Technology (CTμ, Univ Lyon 1). Observations were performed with a Jeol 1400 Flash microscope operated at 200 kV, and equipped with a Gatan Rio 16 digital camera.

Correlative light scanning electron microscopy (CLEM). CLEM was performed in collaboration with the Center for Microstructure Technology (CTμ, Univ Lyon 1). Cells were

plated on standard square coverslips ITO (22x22mm), and fixed with PFA 4% 20 min. After three washes with phosphate buffer 0.2M pH 7.2 for 20min, saturation was achieved using phosphate buffer with 3% BSA and 0.3% Triton X-100 for 45min. Incubation with primary antibodies and washings were performed as mentioned in the section "Immunofluorescence". AlexaFluor-488 Fluoronanogold (FluoroNanogold™, Nanoprobes, #7201) was diluted at 1:100 in phosphate buffer with 1% BSA and 0.2% Tween-20, and incubated for 1h at RT. After washings, coverslips were mounted on a "Shuttle and Find" Zeiss device, and the observation was done with a Zeiss confocal LSM800 microscope. After confocal observation, coverslips were washed three times with H_2O. Then silver enhancement was performed, using the HQ silver enhancement kit (Nanoprobes, #2012) for 5 minutes. After H_2O washings, cells were incubated with 1% final OsO4 in PBS 0.1M pH 7.2, for 45min. After H_2O washings, cells were incubated overnight with 20% acetone in H_2O. The following day, 100% acetone was added for 1h, followed by critical point drying for 2h. SEM imaging was then performed at the Center for Microstructure Technology (CTμ, Univ Lyon 1), using a scanning electron microscope Zeiss Merlin Compact VP.

Statistical methods. Normality test was performed using the Shapiro-Wilk test. Mean comparisons of two samples were performed with an unpaired two-sided Student's t-test with Welch's correction. One-way Anova with post-hoc Tukey test, or with Dunnett's correction test, or with non-parametric Kruskal-Wallis test, or a one-way Welch and Brown-Forsythe ANOVA were used, when multiple comparisons were performed. Statistical analyses were performed using GraphPad Prism software (La Jolla, CA). Significant p values are indicated by asterisks in the figures (* $p<0.05$; ** $p<0.01$; *** $p<0.001$, **** $p<0.0001$).

References to Supplementary Materials & Methods, Figures and Tables.

1. B. Guyot, F. Clément, Y. Drouet, X. Schmidt, S. Lefort, E. Delay, I. Treilleux, J.-P. Foy, S. Jeanpierre, E. Thomas, J. Kielbassa, L. Tonon, H. H. Zhu, P. Saintigny, W.-Q. Gao, A. de la Fouchardiere, F. Tirode, A. Viari, J.-Y. Blay, V. Maguer-Satta, An Early Neoplasia Index (ENI10), Based on Molecular Identity of CD10 Cells and Associated Stemness Biomarkers, is a Predictor of Patient Outcome in Many Cancers. *Cancer Res. Commun.* **3**, 1966–1980 (2023).

2. P.-A. Vidi, M. J. Bissell, S. A. Lelièvre, Three-dimensional culture of human breast epithelial cells: the how and the why. *Methods Mol. Biol.* **945**, 193–219 (2013).

3. Y. Perez-Riverol, Q.-W. Xu, R. Wang, J. Uszkoreit, J. Griss, A. Sanchez, F. Reisinger, A. Csordas, T. Ternent, N. Del-Toro, J. A. Dianes, M. Eisenacher, H. Hermjakob, J. A. Vizcaíno, PRIDE Inspector Toolsuite: Moving Toward a Universal Visualization Tool for Proteomics Data Standard Formats and Quality Assessment of ProteomeXchange Datasets. *Mol. Cell. Proteomics MCP* **15**, 305–317 (2016).

4. Y. Perez-Riverol, C. Bandla, D. J. Kundu, S. Kamatchinathan, J. Bai, S. Hewapathirana, N. S. John, A. Prakash, M. Walzer, S. Wang, J. A. Vizcaíno, The PRIDE database at 20 years: 2025 update. *Nucleic Acids Res.* **53**, D543–D553 (2025).

Supplementary figures and tables to :

Tunneling nanotubes propagate a BMP-dependent preneoplastic state.

Cristina Cuella Martin[1,2,3], Thanh Thuy Nguyen * [1,2,3], Alexia Bertin * [1,2,3], Kevin Geistlich[1,2,3,4], Boris Guyot[1,2,3], Sylvain Lefort[1,2,3], Emmanuel Delay[1,2,3,4], Charline Dalverny[3,5], Alice Boissard[6], Cécile Henry[6], François Guillonneau[6,7,8], Eve-Isabelle Pécheur [§* 1,2,3] and Véronique Maguer-Satta [§* 1,2,3,4]

1. CNRS UMR5286, Centre de Recherche en Cancérologie de Lyon, 69008 Lyon, France;
2. Inserm U1052, Centre de Recherche en Cancérologie de Lyon, 69008 Lyon, France;
3. Université Claude Bernard Lyon 1, Lyon, France;
4. Centre Léon Bérard, 69008 Lyon, France;
5. Centre Technologique des Microstructures, 69622 Villeurbanne, France;
6. Prot'ICO proteomics facility, Institut de Cancérologie de l'Ouest, 49055 Angers, France,
7. Nantes Université, Inserm, CNRS, CRCI2NA, U1307, UMR6075, 44000 Nantes, France;
8. Equipe Labellisée Ligue Contre le Cancer, Paris, France.

* These authors contributed equally; § Co-corresponding authors

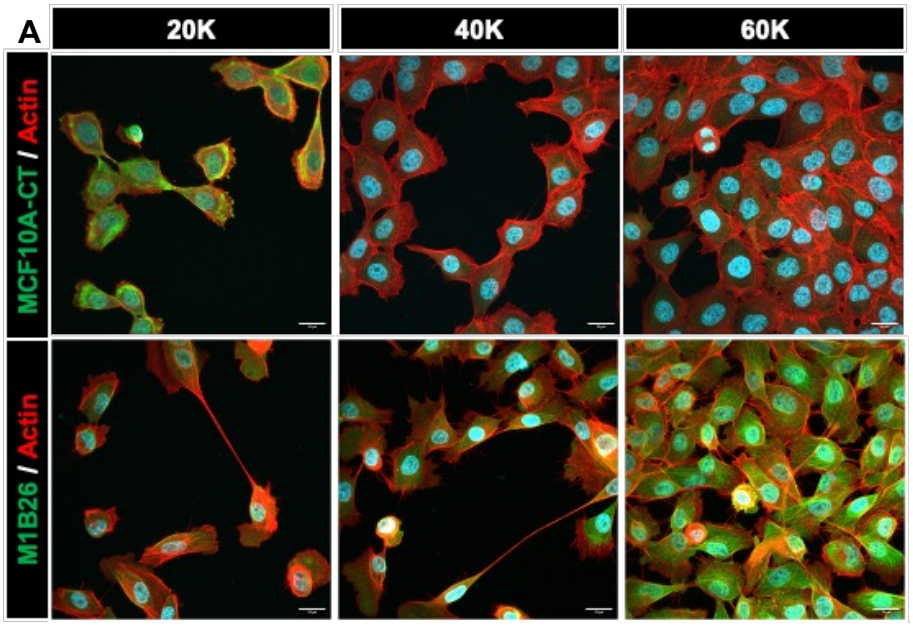
A
20K
40K
60K
MCF10A-CT / Actin
M1B26 / Actin

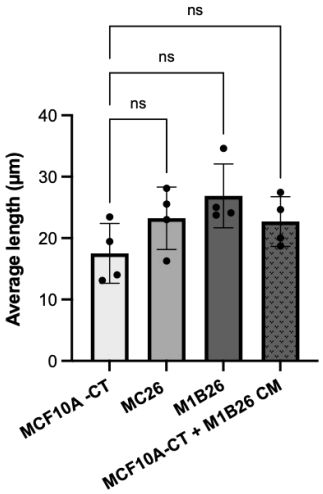
B
ns
ns
ns
Average length (µm)
40
30
20
10
0
MCF10A -CT
MC26
M1B26
MCF10A-CT + M1B26 CM

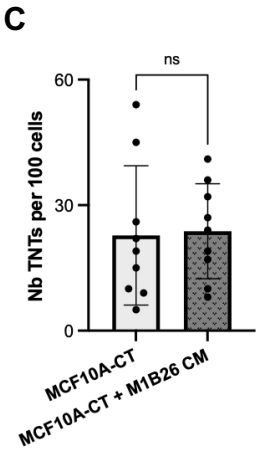
C
ns
Nb TNTs per 100 cells
60
30
0
MCF10A-CT
MCF10A-CT + M1B26 CM

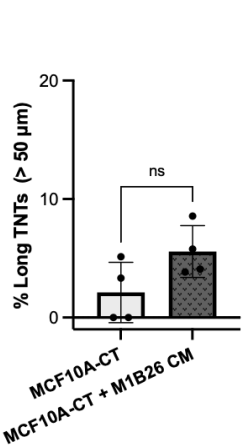
D
ns
% Long TNTs (> 50 µm)
20
10
0
MCF10A-CT
MCF10A-CT + M1B26 CM

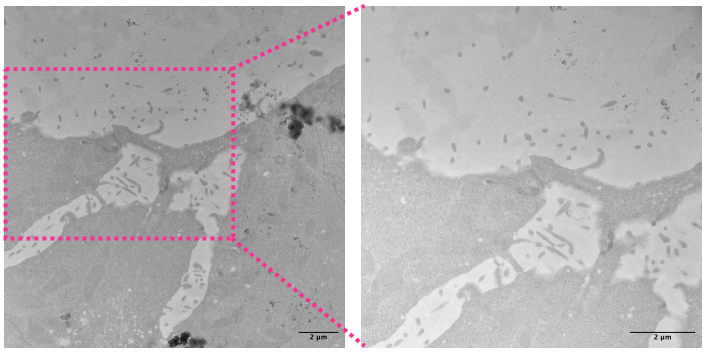
E

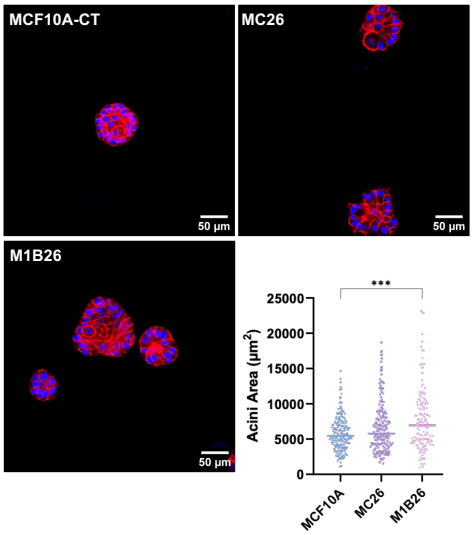
F
MCF10A-CT
MC26
M1B26
50 µm
50 µm
50 µm
***
Acini Area (µm²)
25000
20000
15000
10000
5000
0
MCF10A
MC26
M1B26

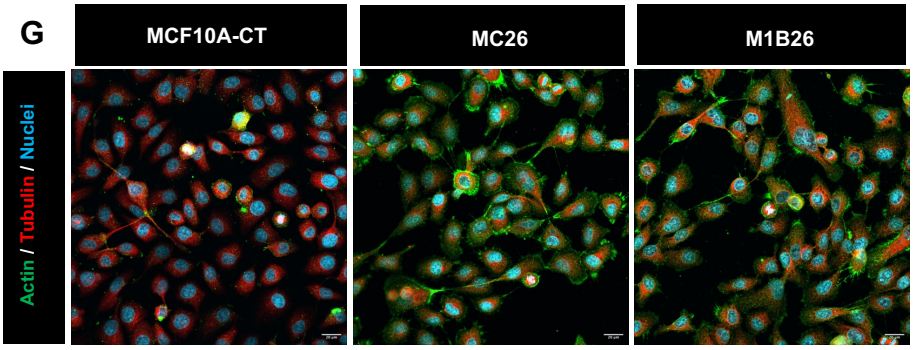
G
MCF10A-CT
MC26
M1B26
Actin / Tubulin / Nuclei

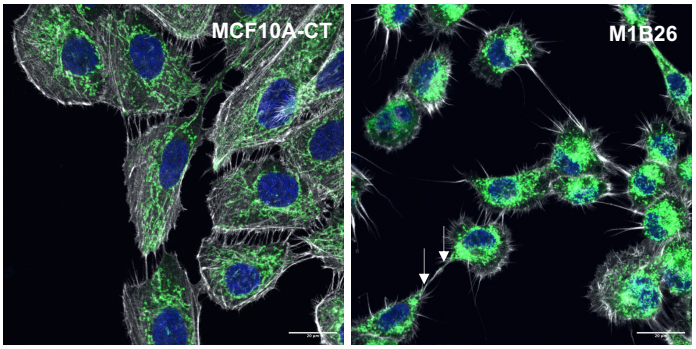
H
MCF10A-CT
M1B26

Figure S1

Figure S1. A, Representative immunofluorescence images of actin (red) and tubulin (green) in MCF10A-CT and M1B26 cells, plated at sub-confluent cell densities (20, 40 and 60K, respectively 20,000;40,000 or 60,000 cells/cm^2), and observed by Airyscan confocal microscopy. Nuclei, Hoechst labeling (blue). Scale bars, 20 µm. B,C,D, Quantification of TNT average length (B, n = 4 biological replicates), TNT number *per* 100 cells (C, n = 9 biological replicates), and % of long TNTs (D; > 50 µm; n = 4 biological replicates) for indicated cell conditions (MCF10A-CT+M1B26 CM : MCF10A-CT cells incubated for 48h with conditioned medium of M1B26 cells). Ten Z-stacks of 10 sections each were taken *per* condition, and 100 cells minimum *per* experiment were counted. TNTs were counted and measured in each Z-stack. Error bars depict SD. Statistical significance was calculated using a one-way ANOVA with post-hoc Tukey test (B) or an unpaired two-sided Student's t test with Welch's correction (C,D). Ns, not significant. E, TEM images of a close-ended TNT linking two M1B26 cells via a Gap junction. Scale bars, 2 µm. F, Immunofluorescence images of actin (red) in acini grown from indicated cell lines. See Methods for acini formation. Nuclei, blue. Scale bars, 50 µm. Bottom right, acini area (in µm^2). Statistiscal significance was calculated using a one-way ANOVA with post-hoc Tukey test (only *** $p < 0.001$ is indicated). G, Immunofluorescence images of actin (green) and tubulin (red) in indicated cell lines. Nuclei, blue. Scale bars, 20 µm. H, Immunofluorescence images of mitochondria (green, Mitotracker™), and actin (grey) in indicated cell lines. Nuclei, blue. Scale bars, 20 µm. All fluorescence observations were performed with a confocal Airyscan Zeiss microscope.

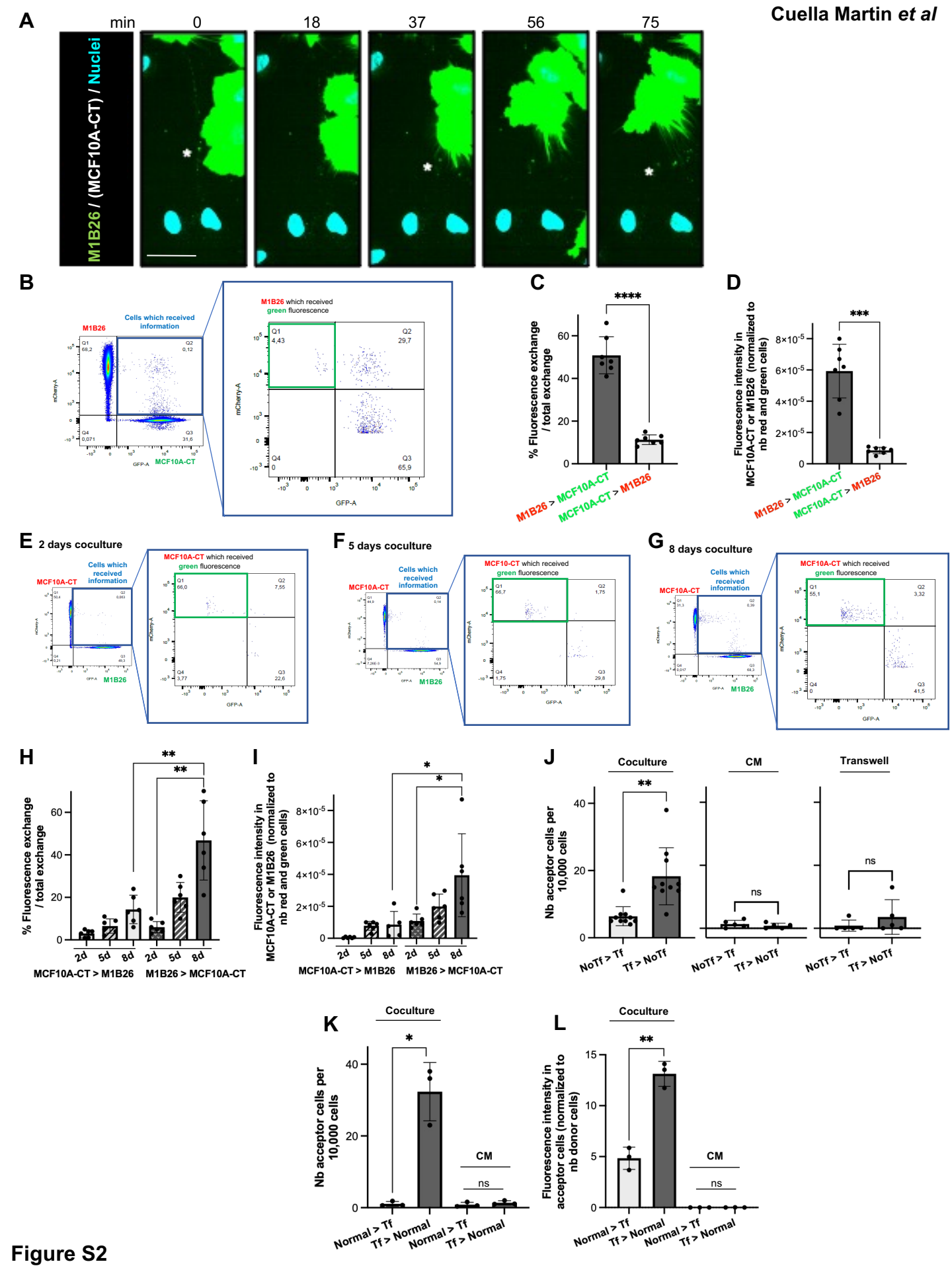
A
min
0
18
37
56
75
M1B26 / (MCF10A-CT) / Nuclei
B
M1B26
Cells which received information
MCF10A-CT
M1B26 which received green fluorescence
C
% Fluorescence exchange / total exchange
****
M1B26 > MCF10A-CT
MCF10A-CT > M1B26
D
Fluorescence intensity in MCF10A-CT or M1B26 (normalized to nb red and green cells)
***
E 2 days coculture
F 5 days coculture
G 8 days coculture
MCF10-CT which received green fluorescence
MCF10A-CT which received green fluorescence
H
2d
5d
8d
MCF10A-CT > M1B26
M1B26 > MCF10A-CT
I
J
Coculture
CM
Transwell
Nb acceptor cells per 10,000 cells
NoTf > Tf
Tf > NoTf
ns
K
Normal > Tf
Tf > Normal
L
Fluorescence intensity in acceptor cells (normalized to nb donor cells)

Figure S2

Figure S2. A, Time-lapse snapshots of green material trafficking within a TNT bulge (*), from GFP (green) M1B26 to MCF10A-CT cells after 48h in coculture. Nuclei, turquoise blue. Scale bar, 100 µm. Images were recorded for 75 min, with one image every 18 min. For movie source data, see Movie S1. B, Flow cytometry analysis of an 8-day coculture of red M1B26 and green MCF10A-CT cells. C,D, Quantification of the percentage of exchange (C) and fluorescence intensity (D), of the indicated transfer. Error bars depict SD. Statistical significance was calculated using an unpaired Student's two-sided t test with Welch's correction (n = 7 biological replicates; *** $p < 0.001$; **** $p < 0.0001$). E,F,G, Flow cytometry analysis of 2 (E), 5 (F) or 8 (G) days of coculture of green M1B26 and red MCF10A-CT cells. H,I, Percentage of material exchange (H) and fluorescence intensity (I), of the indicated transfer after 2, 5 or 8 days of coculture. Error bars are SD. Statistical significance was calculated using a one-way ANOVA with post-hoc Tukey test (n = 6 biological replicates; * $p < 0.05$; ** $p < 0.01$). For clarity, only statistical significance is shown. J, Quantification of the number of acceptor cells *per* 10,000 cells, in standard (10 biological replicates) or Transwell cocultures (5 biological replicates), or in conditioned medium (5 biological replicates), for the indicated transfer involving MCF10A-CT (NoTf) and M1B26 (Tf) cells. Error bars are SD. Statistical significance was calculated using an unpaired Student's two-sided t test with Welch's correction (ns, not significant; ** $p < 0.01$). K,L, Quantification of the number of acceptor cells *per* 10,000 cells (K), and fluorescence intensity (L), in cocultures or with conditioned medium, for the indicated transfer involving normal human primary mammary (normal) and M1B26 cells (Tf). Error bars are SD. Statistical significance was calculated using an unpaired Student's two-sided t test with Welch's correction (n = 3 biological replicates; ns, not significant; * $p < 0.05$; ** $p < 0.01$).

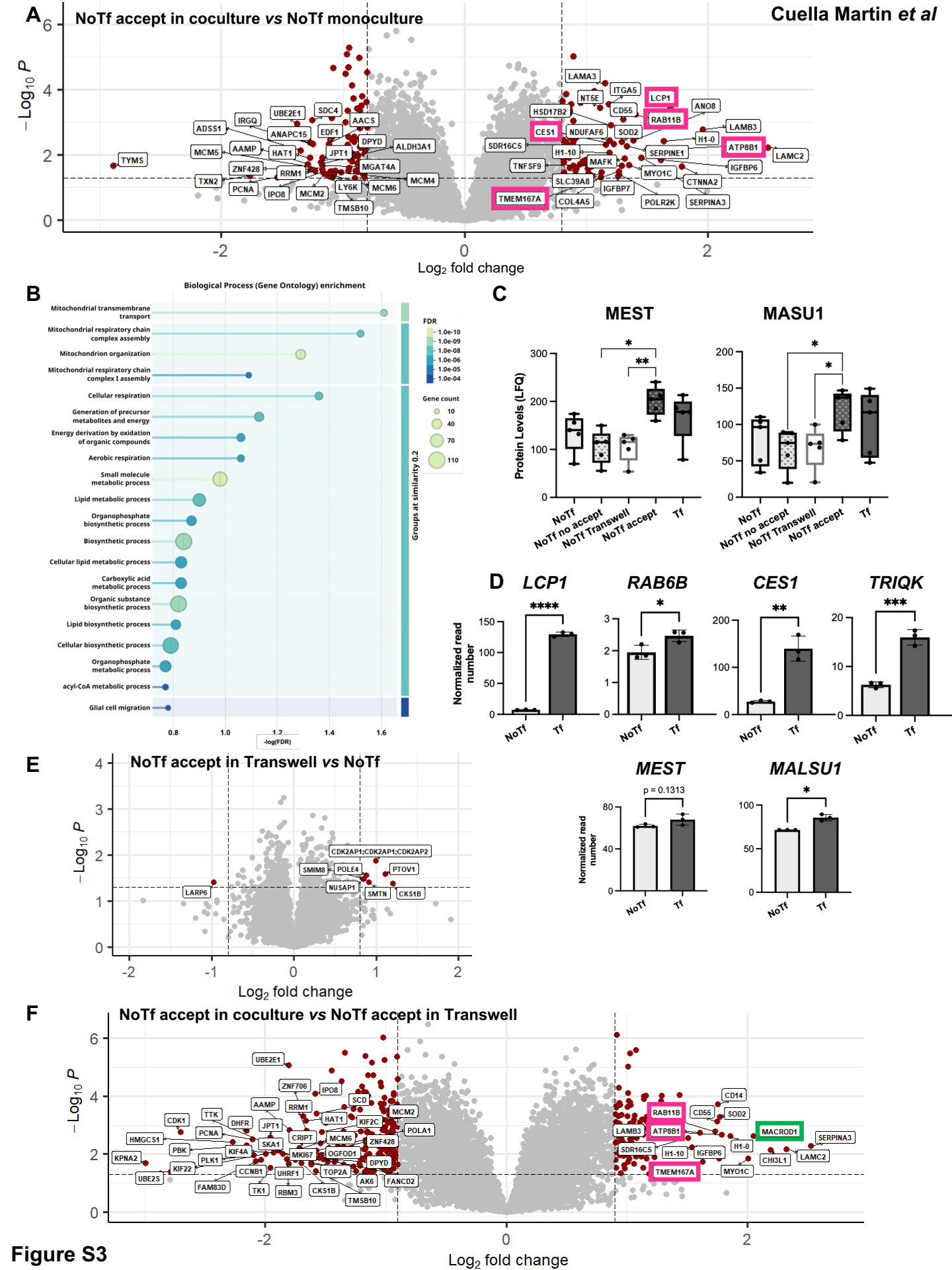
A
NoTf accept in coculture vs NoTf monoculture
−Log10 P
Log2 fold change
B
Biological Process (Gene Ontology) enrichment
Mitochondrial transmembrane transport
Mitochondrial respiratory chain complex assembly
Mitochondrion organization
Mitochondrial respiratory chain complex I assembly
Cellular respiration
Generation of precursor metabolites and energy
Energy derivation by oxidation of organic compounds
Aerobic respiration
Small molecule metabolic process
Lipid metabolic process
Organophosphate biosynthetic process
Biosynthetic process
Cellular lipid metabolic process
Carboxylic acid metabolic process
Organic substance biosynthetic process
Lipid biosynthetic process
Cellular biosynthetic process
Organophosphate metabolic process
acyl-CoA metabolic process
Glial cell migration
-log(FDR)
FDR
Gene count
Groups at similarity 0.2
C
MEST
MASU1
Protein Levels (LFQ)
NoTf
NoTf no accept
NoTf Transwell
NoTf accept
Tf
D
LCP1
RAB6B
CES1
TRIQK
Normalized read number
NoTf
Tf
E
NoTf accept in Transwell vs NoTf
−Log10 P
Log2 fold change
MEST
MALSU1
p = 0.1313
Normalized read number
F
NoTf accept in coculture vs NoTf accept in Transwell
−Log10 P
Log2 fold change

Figure S3

Figure S3. A, Volcano plot showing Log_2 enrichment of individual proteins in non-transformed acceptor cells (NoTf accept) in direct coculture, compared to non transformed (NoTf) cells in monoculture. The threshold for the P-value was set at 0.05 and 0.8 for Log2 fold change. The Log_2 fold change threshold was lowered to 0.5 in order to obtain a larger pool of hits, with a minimum of differences between groups. Proteins with a magenta frame are also overexpressed in NoTf accept cells compared to non transformed non acceptor cells (NoTf no accept), in cocultures (see Fig. 3C). B, From a list of 193 proteins upregulated in NoTf accept cells (in coculture) compared to NoTf cells (in monoculture), STRING (https://string-db.org) was used to generate the gene ontology analysis with the biological process subset. C, Box and whiskers plots of Log_2LFQ values (Protein Levels) of MEST and MASU1, for indicated sorted cell populations. Statistical significance was calculated using one-way ANOVA with Dunnett's multiple comparison test (n = 5 biological replicates; * $p < 0.05$; ** $p < 0.01$; *** $p < 0.001$; **** $p < 0.0001$). For clarity, only significant comparisons are shown. D, RNA-sequencing results showing the transcriptomic expression levels of *LCP1, RAB6B, CES1, TRIQK, MEST and MALSU1* in MCF10A-CT (NoTf) and M1B26 (Tf) (n = 3 biological replicates). Data deposited on the Gene Expression Omnibus repository, GSE186734 *(1)*. Statistical significance was calculated using an unpaired two-sided Student's t test with Welch's correction (* $p < 0.05$; ** $p < 0.01$; *** $p < 0.001$; **** $p < 0.0001$). E,F, Volcano plots showing Log_2 enrichment of individual proteins in NoTf accept in Transwell coculture compared to NoTf cells in monoculture (E), and in NoTf accept cells in direct coculture compared to NoTf accept cells in Transwell coculture (F). Proteins with a magenta frame are also overexpressed in NoTf accept cells compared to NoTf no accept cells, in cocultures (see Fig. 3B), and the protein with a green frame is found overexpressed only in NoTf accept cells in direct coculture compared to NoTf accept cells in Transwell coculture. The threshold for the P-value was set at 0.05 and 0.8 for Log2 fold change. The Log_2 fold change threshold was lowered to 0.5 in order to obtain a larger pool of hits, with a minimum of differences between groups.

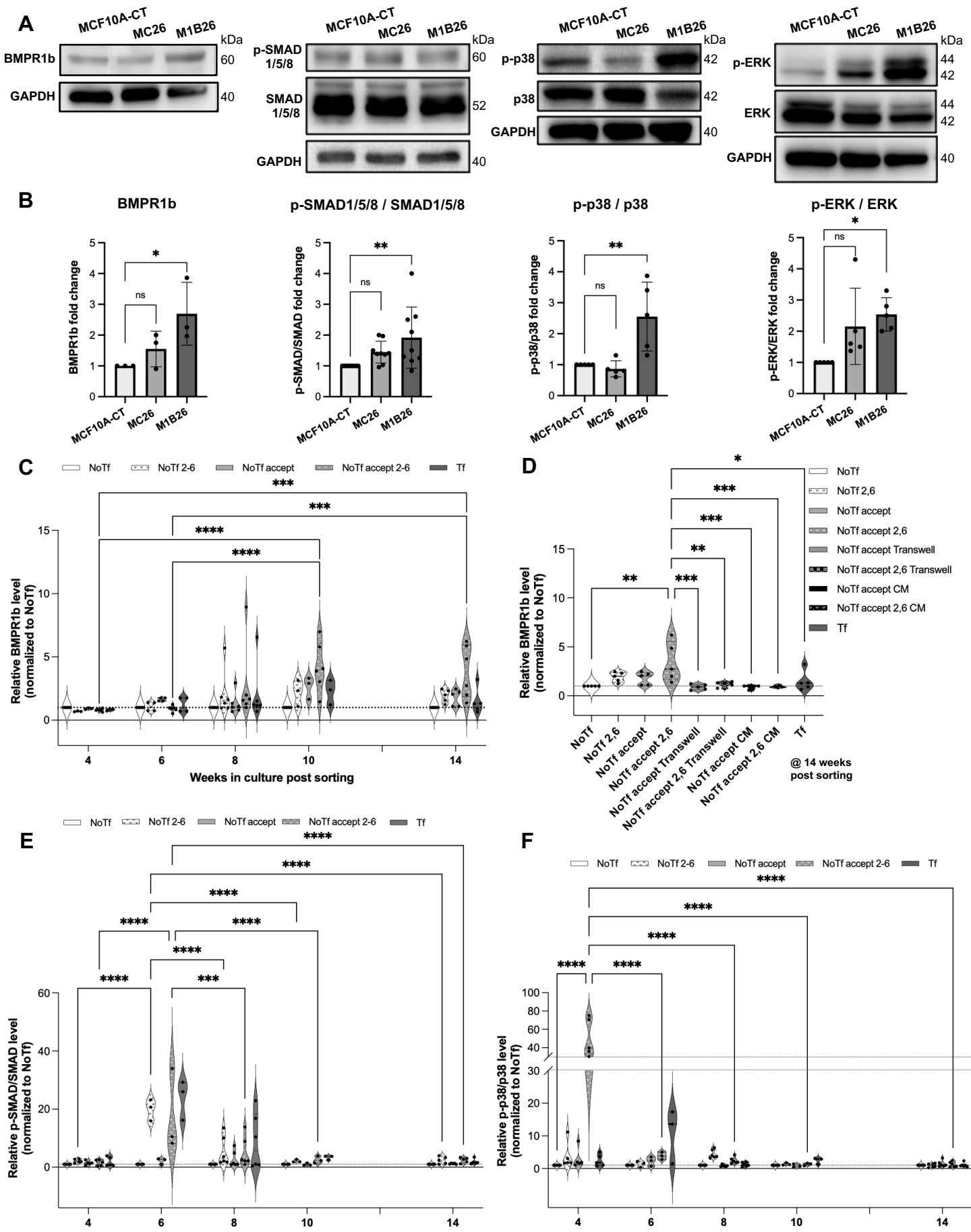
A
MCF10A-CT
MC26
M1B26
kDa
BMPR1b
GAPDH
60
40
p-SMAD 1/5/8
SMAD 1/5/8
52
p-p38
p38
42
p-ERK
ERK
44
B
BMPR1b
p-SMAD1/5/8 / SMAD1/5/8
p-p38 / p38
p-ERK / ERK
BMPR1b fold change
p-SMAD/SMAD fold change
p-p38/p38 fold change
p-ERK/ERK fold change
ns
C
NoTf
NoTf 2-6
NoTf accept
NoTf accept 2-6
Tf
Relative BMPR1b level (normalized to NoTf)
Weeks in culture post sorting
D
NoTf 2,6
NoTf accept 2,6
NoTf accept Transwell
NoTf accept 2,6 Transwell
NoTf accept CM
NoTf accept 2,6 CM
@ 14 weeks post sorting
E
Relative p-SMAD/SMAD level (normalized to NoTf)
F
Relative p-p38/p38 level (normalized to NoTf)

Figure S4

Figure S4. A, From left to right : Immunoblots of indicated proteins, in MCF10A-CT, MC26 and M1B26 cells. B, From left to right : quantification of immunoblots shown in A. Error bars are SD. Statistical significance was calculated using a one-way ANOVA with post-hoc Tukey test (biological replicates : n = 3 for BMPR1b, n = 9 for p-SMAD1/5/8 / SMAD1/5/8, n = 5 for p-p38/p38 and p-ERK/ERK ; ns, not significant, * $p < 0.05$; ** $p < 0.01$). Data are mean ± SD. C, Quantification of BMPR1b immunoblots, from lysates of cells grown for indicated time post flow cytometry sorting (see schematic Fig. 4G). Violin plots of 3 to 6 biological replicates, with NoTf and NoTf 2-6, MCF10A-CT cells grown in the absence or presence of BMP2/IL6, respectively; NoTf accept and NoTf accept 2-6, MCF10A cells grown in coculture with M1B26 cells, and cultured in the absence or presence of BMP2/IL6 post-sorting, respectively; Tf, M1B26 cells. NoTf conditions are set at 1. Statistical significance was calculated using a two-way ANOVA with Tukey's multiple comparison test. For clarity, only significant comparisons are shown. D, Quantification of BMPR1b immunoblots performed on indicated cells, 14 weeks post sorting, with NoTf conditions set at 1. Violin plot of 5 biological replicates. Statistical significance was calculated using a one-way ANOVA with post-hoc Tukey test, with only significant comparisons shown (* $p < 0.05$; ** $p < 0.01$; *** $p < 0.001$). Legend as in C, with : Transwell, coculture in Transwell; CM, NoTf (MCF10A-CT) cells grown in conditioned medium of M1B26 cells, sorted and grown in the absence or presence of BMP2/IL6. E,F, Quantification of p-SMAD1/5/8/SMAD1/5/8 (E) and p-p38/p38 (F) immunoblots, on same samples as in B.

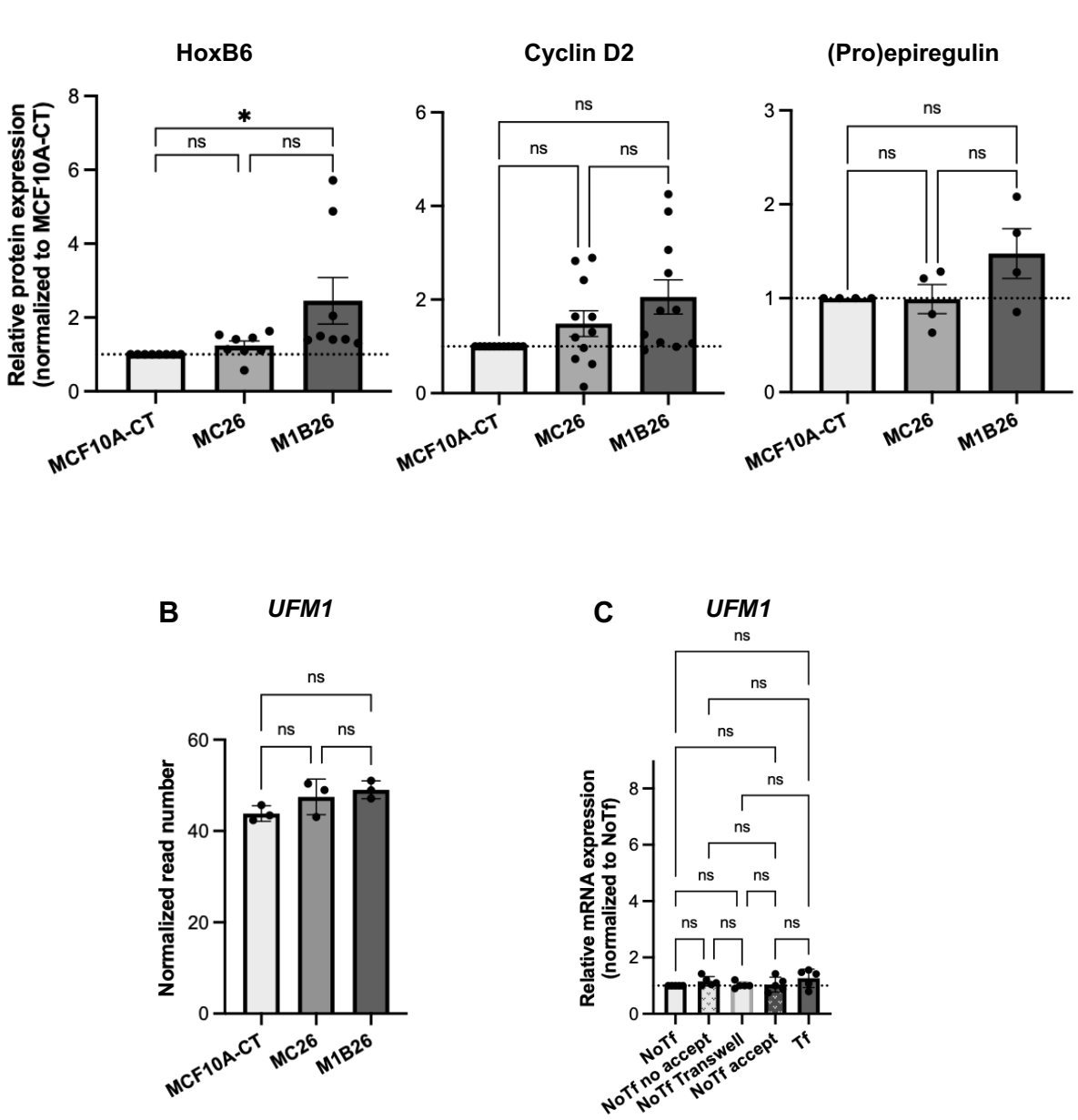
A
HoxB6
Cyclin D2
(Pro)epiregulin
Relative protein expression
(normalized to MCF10A-CT)
*
ns
MCF10A-CT
MC26
M1B26
B
UFM1
Normalized read number
C
UFM1
Relative mRNA expression
(normalized to NoTf)
NoTf
NoTf no accept
NoTf Transwell
NoTf accept
Tf

Figure S5

Figure S5. A, Quantification of immunoblots of HoxB6, Cyclin D2 and (pro)-epiregulin in MCF10A-CT, MC26 and M1B26 cells, with normalization against MCF10A-CT levels. Data are mean ± SEM (Biological replicates : n = 8 for HoxB6; n = 11 for cyclin D2; n = 4 for (pro)epiregulin). Statistical significance was calculated using a one-way ANOVA with post-hoc Tukey test (ns, not significant; * $p < 0.05$). B, RNA-sequencing results showing the transcriptomic expression levels of UFM1 in indicated cell lines (n = 3 biological replicates). Data deposited on the Gene Expression Omnibus repository, GSE186734 *(1)*. Error bars represent SD. Statistical significance was calculated using a one-way ANOVA with post-hoc Tukey test (ns, not significant). C, RT-qPCR measurements of UFM1 mRNA in indicated cell populations, with the expression in NoTf cells set at to 1. Error bars represent SD. Statistical significance was calculated using a one-way ANOVA with post-hoc Tukey test (n = 5 biological replicates; ns, not significant).

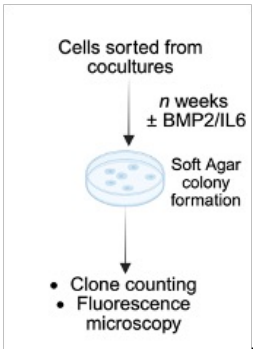
A
Cells sorted from cocultures
n weeks
± BMP2/IL6
Soft Agar colony formation
Clone counting
Fluorescence microscopy

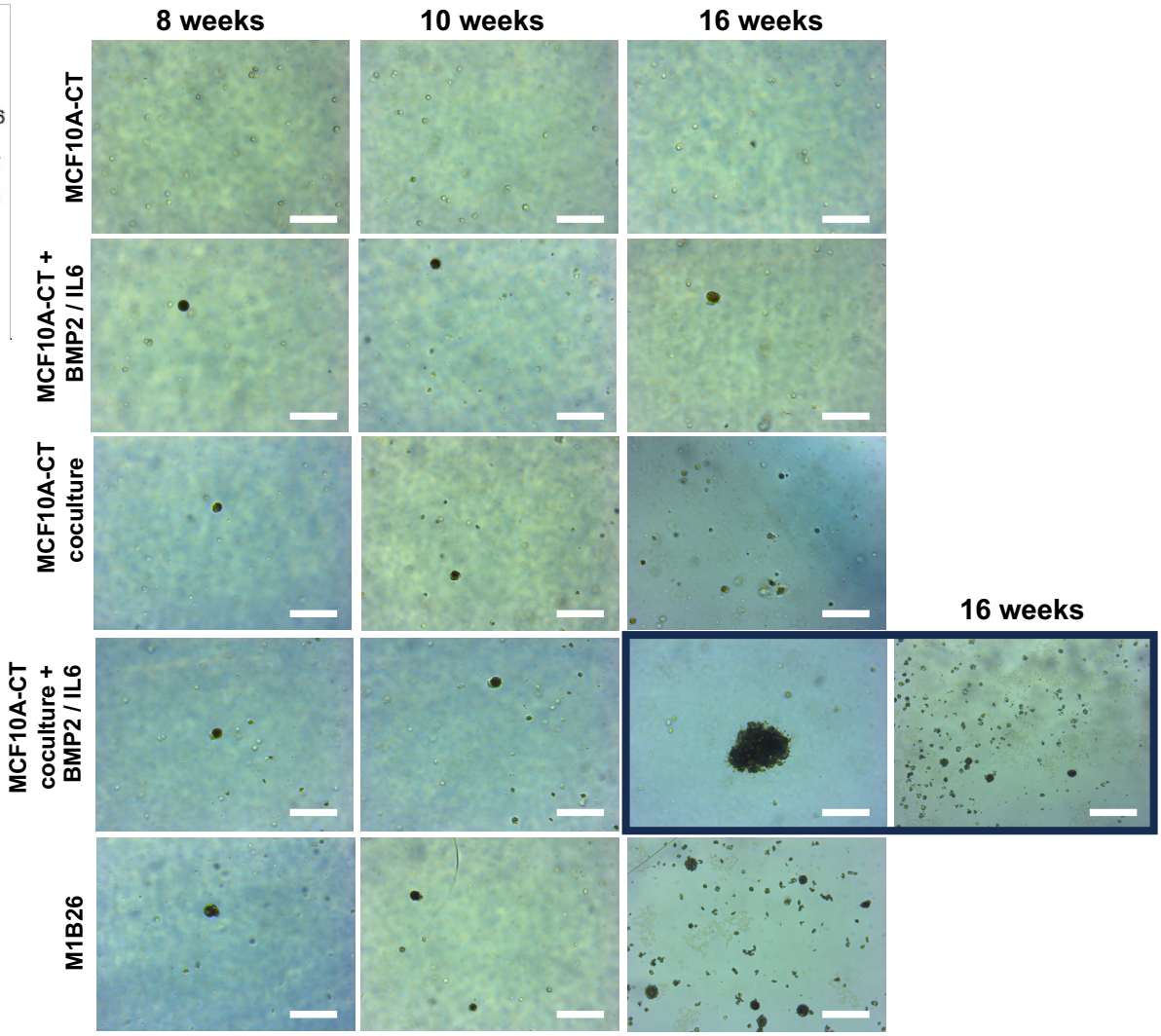
B
8 weeks
10 weeks
16 weeks
MCF10A-CT
MCF10A-CT + BMP2 / IL6
MCF10A-CT coculture
MCF10A-CT coculture + BMP2 / IL6
16 weeks
M1B26

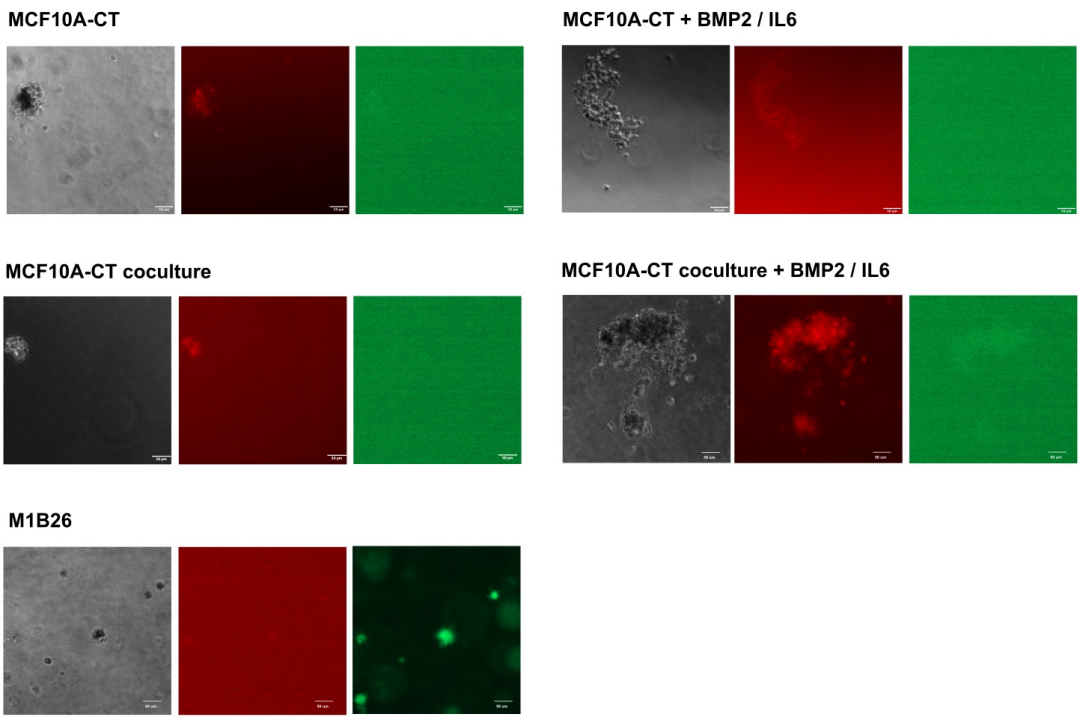
C
MCF10A-CT
MCF10A-CT + BMP2 / IL6
MCF10A-CT coculture
MCF10A-CT coculture + BMP2 / IL6
M1B26

Figure S6

Figure S6. A, Schematic of long-term soft agar colony formation assays. B, Representative bright-field images of soft agar clones after indicated weeks in the absence or presence of BMP2/IL6. Pictures with a dark frame are representative of big or small clones observed for the indicated cell condition. Scale bar represents 200 μm. C, Representative images of soft agar clones obtained from indicated cells and conditions, and observed by epifluorescence microscopy. After sorting by flow cytometry, cells were grown in the absence or presence of BMP2/IL6 for several weeks (see Fig. 5B), and at given time points, collected to perform soft agar colony formation assay (see panel A). Clones shown here were formed from cells grown for 16 weeks post sorting. From left to right : bright field, mCherry, GFP. Scale bars are 50 μm.

Table S1. The ten most differentially expressed genes (from proteomic analyses) between NoTf accept and NoTf no accept cells, in direct coculture conditions, showing Log_2 enrichment of individual proteins (LogFC) and corresponding p-value (see legend to Fig. S3A for more details).

UP			DOWN		
Protein	**LogFC**	**P value**	**Protein**	**LogFC**	**P value**
CES1	0.889122589477469	0.0141628941286904	ABHD14B	-1.00315026985703	0.000980307865197619
MEST	0.932759743282637	0.00188098627865132	PHPT1	-1.01510146569795	0.00356732439665008
RAB6B	0.933811759708842	0.0109448236612979	ENSA	-1.02370657619597	0.0161174249871283
CAV2	0.99732226024381	0.0408269875434742	JPT2	-1.10698538807139	0.00935740869041231
COX7C	1.07266576845297	0.010209697566701	JPT1	-1.10835843431927	0.00793600149391597
LCP1	1.09840574413178	0.00154609002947331	OGFOD2	-1.1132683686952	0.0415033799952983
SYT8	1.17672071307107	0.043954377019624	TMSB10	-1.14967105039942	0.00540682517524317
RAB11B	1.3714054705064	0.000626507681921401	ZNF706	-1.15566233765069	0.00111603705555586
TMEM167A	1.45520736261194	0.0219143303939675	EEF1AKMT2	-1.27111422803223	0.00946055818632448
ATP8B1	2.09279285090789	0.000411271663574841	DAP	-1.40988711973543	0.0455217421389704

Table S2. The ten most differentially expressed genes (from proteomic analyses) between NoTf accept in direct coculture and NoTf accept in Transwell coculture conditions, showing Log_2 enrichment of individual proteins (LogFC) and corresponding p-value (see legend to Fig. S3A for more details).

UP		
Protein	**LogFC**	**P value**
CD14	1.75212297141304	0.000191011658635565
IGFBP6	1.76618122025904	0.0139229645066205
SOD2	1.77111253782108	0.000523439457102529
LAMB3	1.78650743040783	0.00216132909781278
H1-0	1.85763513264292	0.00242570948335453
MYO1C	2.0046600551578	0.0143021854781629
MACROD1	2.04828979371154	0.00240255771521197
CHI3L1	2.18947902717664	0.00727017238146173
LAMC2	2.3234530990449	0.00671123053131829
SERPINA3	2.52280933849719	0.00535426160167644

DOWN		
Protein	**LogFC**	**P value**
TYMS	-3.27748800106074	0.0134778717596743
UBE2T	-3.13040276466167	0.023473217872104
KPNA2	-2.98962869371859	0.0202660294833902
UBE2S	-2.78386369927229	0.0408842282474856
CDK1	-2.70314055151148	0.0017239046757659
HMGCS1	-2.26815542277271	0.003911088063124
DHFR	-2.15668666737884	0.0015530984577745
PBK	-2.15384894310531	0.00508833653275616
PCNA	-2.10549674961135	0.00314193588565591
PLK1	-2.09690800691763	0.0106792923363495

Table S3. Pathway analyses were performed using STRING (https://string-db.org/) with the Biological Process category from the Gene Ontology collection. For the search of BMP and p38 pathways targets, a combination of several pathways from different collections have been compiled (GOBP_POSITIVE_REGULATION_OF_BMP_SIGNALING_PATHWAY ; GOBP_REGULATION_OF_BMP_SIGNALING_PATHWAY ; GOBP_RESPONSE_TO_BMP ; PID_BMP_PATHWAY ; BIOCARTA_P38MAPK_PATHWAY ; GOBP_P38MAPK_CASCADE ; GOBP_REGULATION_OF_P38MAPK_CASCADE ; REACTOME_P38MAPK_EVENTS ; WP_P38_MAPK_SIGNALING).

#Category	Term ID	Term description	Observed gene counts	Background gene counts	Strength	Signal	False discovery rate (FDR)	Matching proteins in network (IDs)	Matching proteins in network (labels)
GO Process	GO:0007166	Cell surface receptor signaling pathway	7	2040	0.93	0.67	0.0068	9606.ENSP00000264110,9606.ENSP00000280377,9606.ENSP00000339191,9606.ENSP00000348461,9606.ENSP00000356070,9606.ENSP00000379975,9606.ENSP00000414147	ATF2,USP15,CAV1,RAC1,MAPKAPK2,ILK,SPART
GO Process	GO:0071363	Cellular response to growth factor stimulus	5	473	1.42	1.01	0.0068	9606.ENSP00000264110,9606.ENSP00000280377,9606.ENSP00000339191,9606.ENSP00000356070,9606.ENSP00000414147	ATF2,USP15,CAV1,MAPKAPK2,SPART
GO Process	GO:0007167	Enzyme-linked receptor protein signaling pathway	5	641	1.28	0.92	0.0075	9606.ENSP00000264110,9606.ENSP00000280377,9606.ENSP00000348461,9606.ENSP00000356070,9606.ENSP00000414147	ATF2,USP15,RAC1,MAPKAPK2,SPART
GO Process	GO:0006468	Protein phosphorylation	5	736	1.22	0.82	0.0119	9606.ENSP00000264110,9606.ENSP00000280377,9606.ENSP00000339191,9606.ENSP00000356070,9606.ENSP00000379975	ATF2,USP15,CAV1,MAPKAPK2,ILK
GO Process	GO:0030509	BMP signaling pathway	3	92	1.9	1.03	0.0156	9606.ENSP00000264110,9606.ENSP00000280377,9606.ENSP00000414147	ATF2,USP15,SPART
GO Process	GO:0030510	Regulation of BMP signaling pathway	3	104	1.85	0.97	0.0191	9606.ENSP00000339191,9606.ENSP00000379975,9606.ENSP00000414147	CAV1,ILK,SPART
GO Process	GO:0038066	p38MAPK cascade	2	13	2.58	1.01	0.0223	9606.ENSP00000264110,9606.ENSP00000356070	ATF2,MAPKAPK2
GO Process	GO:0071310	Cellular response to organic substance	6	2019	0.86	0.51	0.0356	9606.ENSP00000264110,9606.ENSP00000280377,9606.ENSP00000339191,9606.ENSP00000356070,9606.ENSP00000379975,9606.ENSP00000414147	ATF2,USP15,CAV1,MAPKAPK2,ILK,SPART

Table S4. Primers for RT-qPCR used in this study.

HPRT FW	TGACCTTGATTTATTTTGCATACC
HPRT RV	CGAGCAAGACGTTCAGTCCT
TBP FW	TGTATCCACAGTGAATCTTGGTTG
TBP RV	GGTTCGTGGCTCTCTTATCCTC
BMPR1B FW	CTGTGGTCACTTCTGGTTGC
BMPR1B RV	TTCCTTTCTGTGCAGCATTC
EREG FW	TCTGCCTGGGTTTCCATCTT
EREG RV	ATTGACACTTGAGCCACACG
HOXB6 FW	CGTGCAACAGTTCCTCCTTT
HOXB6 RV	GCGTCAGGTAGCGATTGTAGT
CCND2 FW	TGCTGGAGTGGGAACTGGTG
CCND2 RV	ACACAGAGCAATGAAGGTCT
UFM1 FW	AAAGTTCCTGCTGCAACAAGTGC
UFM1 RV	ACACGATCTCTAGGAATAATCCGC
HRAS FW	ACGCACTGTGGAATCTCGGCAG
HRAS RV	TCACGCACCAACGTGTAGAAGG